

1 **Oxysterols drive inflammation via GPR183 during influenza virus and SARS-CoV-2**
2 **infection**

3 Cheng Xiang Foo^{1#}, Stacey Bartlett^{1#}, Keng Yih Chew², Minh Dao Ngo¹, Helle Bielefeldt-
4 Ohmann^{2,3}, Buddhika Jayakody Arachchige⁴, Benjamin Matthews⁴, Sarah Reed⁴, Ran
5 Wang¹, Matthew J. Sweet^{3,5}, Lucy Burr⁶, Jane E. Sinclair², Rhys Parry², Alexander
6 Khromykh^{2,3}, Kirsty R. Short^{2,3}, Mette Marie Rosenkilde⁷ and Katharina Ronacher^{1,3*}

7 ¹Mater Research Institute, Translational Research Institute, The University of Queensland,
8 Brisbane, Australia

9 ²School of Chemistry and Molecular Biosciences, The University of Queensland, Brisbane,
10 Australia

11 ³Australian Infectious Diseases Research Centre, The University of Queensland, Brisbane,
12 Australia

13 ⁴Centre for Clinical Research, The University of Queensland, Brisbane, Australia

14 ⁵Institute for Molecular Bioscience (IMB), IMB Centre for Inflammation and Disease
15 Research, The University of Queensland, Brisbane, Australia

16 ⁶Department of Respiratory Medicine, Mater Adult Hospital, South Brisbane, Queensland,
17 Australia

18 ⁷Department of Biomedical Sciences, University of Copenhagen, Copenhagen, Denmark

19 [#] Contributed equally to this work.

20 ^{*}Correspondence:

21 Katharina Ronacher: Mater Research Institute, Translational Research Institute, 37 Kent
22 Street, Brisbane 4102, QLD, Australia; email: Katharina.Ronacher@mater.uq.edu.au;
23 phone: +61 7 3443 7633

24

25

26

27

28

29 **Author Summary:** Viral infections trigger oxysterol production in the lung, attracting
30 macrophages via GPR183. Blocking GPR183 reduced inflammation and disease severity in
31 SARS-CoV-2 infection, making GPR183 a putative target for therapeutic intervention.

32

33 **Abstract**

34

35 *Rationale:* Severe viral respiratory infections are often characterized by extensive myeloid
36 cell infiltration and activation and persistent lung tissue injury. However, the immunological
37 mechanisms driving excessive inflammation in the lung remain elusive.

38 *Objectives:* To identify the mechanisms that drive immune cell recruitment in the lung during
39 viral respiratory infections and identify novel drug targets to reduce inflammation and disease
40 severity.

41 *Methods:* Preclinical murine models of influenza virus and SARS-CoV-2 infection.

42 *Results:* Oxidized cholesterols and the oxysterol-sensing receptor GPR183 were identified
43 as drivers of monocyte-macrophage infiltration to the lung during influenza virus (IAV) and
44 SARS-CoV-2 infections. Both IAV and SARS-CoV-2 infections upregulated the enzymes
45 cholesterol 25-hydroxylase (CH25H) and cytochrome P450 family 7 subfamily member B1
46 (CYP7B1) in the lung, resulting in local production of the oxidized cholesterols 25-
47 hydroxycholesterol and 7α ,25-dihydroxycholesterol (7α ,25-OHC). Loss-of-function mutation
48 of GPR183, or treatment with a GPR183 antagonist, reduced macrophage infiltration and
49 inflammatory cytokine production in the lungs of IAV- or SARS-CoV-2-infected mice. The
50 GPR183 antagonist also significantly attenuated the severity of SARS-CoV-2 infection by
51 reducing weight loss and viral loads.

52 *Conclusion:* This study demonstrates that oxysterols drive inflammation in the lung and
53 provides the first preclinical evidence for therapeutic benefit of targeting GPR183 during
54 severe viral respiratory infections.

55

56

57 **Introduction**

58 Severe viral respiratory infections including influenza and COVID-19 are associated with
59 extensive myeloid cell recruitment to the lung, which can lead to a cytokine storm, severe
60 tissue injury and the development of acute respiratory distress syndrome (ARDS) (1, 2). A
61 shift in lung macrophage composition and function is associated with COVID-19 severity. A
62 study of >600 hospitalised patients found that in severe cases resident alveolar macrophages
63 were depleted and replaced by large numbers of inflammatory monocytes and monocyte-
64 derived macrophages (3). Rapid monocyte infiltration of the lung during the acute phase of
65 severe acute respiratory coronavirus 2 (SARS-CoV-2) infection is replicated in several animal
66 models (4-6). On the other hand, monocyte recruitment is also an essential component of
67 repair following lung injury (7). Therapeutic approaches are required that balance pro-
68 inflammatory and pro-repair functions of recruited monocytes.

69 Oxidized cholesterols, so called oxysterols, have recently emerged as markers of
70 inflammation in the lung. Oxysterols were increased in bronchoalveolar lavage fluid (BALF)
71 from inflamed airways after allergen challenge and strongly correlated with infiltrating
72 leukocytes (8). They were also increased in the sputum from patients with chronic obstructive
73 pulmonary disease (COPD) correlating with disease severity (9, 10) and in the lungs of mice
74 after lipopolysaccharide (LPS)-induced lung inflammation (9). However, the role of oxysterols
75 in the lung during viral respiratory infections has not been investigated.

76 Oxysterols have a range of properties and receptors sharing a common role in inflammation
77 (11, 12). One of these oxysterol producing pathways leads to the production of 7 α ,25-
78 hydroxycholesterol (7 α ,25-OHC), via cholesterol 25-hydroxylase (CH25H) and cytochrome
79 P450 family 7 subfamily B member 1 (CYP7B1) (12, 13) (**Figure 1A**). 7 α ,25-OHC is the
80 endogenous high affinity agonist of the oxidized cholesterol-sensing G protein-coupled
81 receptor GPR183 (also known as Epstein-Barr virus-induced gene 2; EBI2) (14, 15). GPR183
82 is expressed on cells of the innate and adaptive immune systems, including macrophages,
83 dendritic cells, innate lymphoid cells, eosinophils and T and B lymphocytes (8, 16-18). With
84 its oxysterol ligands GPR183 facilitates the chemotactic distribution of immune cells to
85 secondary lymphoid organs (12, 14, 16, 17). *In vitro* GPR183 mediates migration of human
86 and mouse macrophages towards a 7 α ,25-OHC gradient (19-21).

87 In this study, we hypothesized that viral respiratory infections lead to the production of
88 oxysterols in the lung and that these oxysterols contribute to excessive immune cell infiltration

89 and inflammation. We show here that oxysterols drive GPR183-dependent monocyte
90 infiltration in preclinical models of IAV and SARS-CoV-2 infection. Administration of a
91 GPR183 antagonist significantly reduces inflammation, viral load and disease severity in mice
92 infected with SARS-CoV-2. Accordingly, GPR183 is a putative host target for therapeutic
93 intervention to mitigate disease severity in viral respiratory infections.

94 **Methodology**

95 **Ethics and biosafety**

96 All experiments were approved by the University of Queensland Animal Ethics Committee
97 (MRI-UQ/596/18, AE000186) by the Institutional Biosafety Committee of the University of
98 Queensland (IBC/465B/MRI/TRI/AIBN/2021).

99 **Viral Strains**

100 Virus stocks of A/H1N1/Auckland/1/2009(H1N1) (Auckland/09) were prepared in
101 embryonated chicken eggs. Viral titers were determined by plaque assays on Madin-Darby
102 canine kidney (MDCK) cells as previously described (22). A mouse-adapted SARS-CoV-2
103 strain was obtained through serial passage of SARS-CoV-2 (B.1.351; hCoV-
104 19/Australia/QLD1520/2020, GISAID accession EPI_ISL_968081, collected on 29 December
105 2020, kindly provided by Queensland Health Forensic and Scientific Services). Six $\times 10^4$ PFU
106 of B1.351 was administered intranasally to ketamine-anesthetized mice. Mice were
107 monitored daily for weight loss and clinical signs of disease severity. Four days after
108 inoculation, mice were euthanized, and bronchoalveolar lavage (BAL) was performed. The
109 BALF was subsequently pooled and used to intranasally inoculate a new batch of mice. The
110 process was repeated until a virulent phenotype of the virus was observed as determined by
111 weight loss and clinical signs, which happened after four passages. To determine whether
112 the mouse adapted SARS-CoV-2 acquired mutations sequencing of viral RNA was
113 performed. Briefly, viral RNA was extracted from BALF using the Qiagen Mini kit and the
114 quality confirmed using the Agilent Bioanalyzer with 210 Expert software. Library
115 preparations was performed using the Illumina Stranded Total RNA Ribo Zero Plus kit.
116 Sequencing was performed using the NextSeq Midoutput kit, 125bp paired-end configuration
117 with 19-25 million reads per sample. Sequencing analysis was executed using Galaxy
118 software. Whole-genome sequencing revealed a C to T mutation in position 10804 of the
119 SARS-CoV-2 Beta genome resulting in the NSP5 mutation P252L. This mutation was rapidly
120 selected from 3.4% in the initial virus stock to 8.8% in passage one. From passage two, this

121 mutation reached consensus (60%) and underwent further fixation in passage three at 87%
122 to final frequency of 92% in passage four. A mutation in NSP5 was detected in this mouse
123 adapted SARS-CoV-2 strain (**Figure S1**). BALF of the mice from the fourth passage was
124 subsequently pooled and used to inoculate Vero E6 cells for propagation, creating the viral
125 stocks for our mouse-adapted strain. To verify the virulent phenotype of the mouse-adapted
126 virus was retained after propagation in Vero E6 cells, the cell grown virus was used to
127 inoculate a new batch of mice. The same viral stock was used to infect mice with 8×10^4 PFU
128 for the experiments described.

129 **Bioinformatic analysis of mouse-adapted SARS-CoV-2 sequence data**

130 Base-called fastq files were mapped to the QLD1520 SARS-CoV-2 isolate (GISAID
131 accession EPI_ISL_968081) using Bowtie2 (v2.4.2) (Langmead and Salzberg 2012) under
132 default alignment conditions. Sub consensus variants of alignment files were identified using
133 iVar (v1.2.2) (Grubaugh et al. 2019) with a minimum quality score threshold of 20 and depth
134 of 5000. Coverage of mapped alignment files was determined using samtools (v1.3) depth.
135 Frequencies and coverage of variant positions were manually validated using Integrative
136 Genomics Viewer (Version: 2.7.0) (Thorvaldsdottir, Robinson, and Mesirov 2013). Variant
137 frequencies and alignment depth was visualized using GraphPad Prism (v9.3.1). Raw fastq
138 data generated in this study have been deposited in the Sequence Read Archive hosted by
139 the National Center for Biotechnology Information with accession number PRJNA849351.

140 **Plaque assays**

141 IAV plaque assays were carried out on confluent monolayers of MDCK cells as previously
142 described (22). SARS-CoV-2 plaque assays were carried out on Vero E6 cells as described
143 previously (23).

144 **Mouse models**

145 *Gpr183tm1Lex* were obtained from Lexicon Pharmaceuticals (The Woodlands, USA), back-
146 crossed to a C57BL/6J background and bred in-house at the Biological Resources Facility at
147 the Translational Research Institute, Australia. Eight to 10-week-old C57BL/6J and
148 *Gpr183tm1Lex* (C57BL/6J background; *Gpr183^{-/-}*) mice were anesthetized with isoflurane
149 (4% isoflurane, 0.4 L/min oxygen flow rate) before being inoculated intranasally with 5,500
150 PFU of A/Auckland/01/09 (H1N1). Mice were monitored for weight loss. For SARS-CoV-2
151 infection, C57BL/6J and *Gpr183^{-/-}* mice were anesthetized with ketamine/Xylazine
152 (80mg/kg/5mg/kg) before being inoculated intranasally with 8×10^4 PFU of mouse-adapted
153 SARS-CoV-2 and monitored for weight loss. Lungs were collected at specified timepoints for

154 subsequent downstream analysis. The GPR183 antagonist NIBR189 was administrated from
155 1 dpi. IAV infected mice were sacrificed at 3 dpi and 7 dpi for examination. SARS-CoV-2
156 infected mice were sacrificed at 2 dpi and 5 dpi. Lungs homogenised in DMEM for use in
157 plaque assays and ELISAs. For RNA processing, lungs were collected in TRIzol (Invitrogen).
158 For oxysterol extraction, lungs were collected in methanol. For histological analysis the lungs
159 were fixed in 10% neutral buffered formalin.

160 **RNA isolation and RT-qPCR**

161 Total RNA was isolated using ISOLATE II RNA Mini Kit (Bioline Reagents Ltd., London, UK)
162 as previously described (24). The list of primers (Sigma Aldrich) is provided in **Table S1**. The
163 relative expression (RE) of each gene using the $2^{-\Delta Ct}$ method, normalizing to the reference
164 gene (Hypoxanthine-guanine phosphoribosyltransferase; HPRT).

165 **Oxysterol extraction from lung tissues**

166 The oxysterol extraction and quantification method was adapted from Ngo et al. (24). Lung
167 lobes from IAV and SARS-CoV-2-infected mice were homogenized in methanol. Oxysterols
168 were extracted using a 1:1 dichloromethane:methanol solution containing 50 µg/mL BHT in
169 a 30°C ultrasonic bath. Tubes were flushed with nitrogen to displace oxygen, sealed with a
170 polytetrafluoroethylene (PTFE)-lined screw cap, and incubated at 30°C in the ultrasonic bath
171 for 10 mins. Following centrifugation (3,500 rpm, 5 min, 25°C), the supernatant from each
172 sample was decanted into a new tube. For liquid-liquid extraction, Dulbecco's phosphate-
173 buffered saline (DPBS) was added to the supernatant, agitated and centrifuged at 3,500 rpm
174 for 5 mins at 25°C. The organic layer was recovered and evaporated under nitrogen using a
175 27-port drying manifold (Pierce; Fisher Scientific, Fair Lawn, NJ). Oxysterols were isolated
176 by solid-phase extraction (SPE) using 200 mg, 3 mL aminopropyl SPE columns (Biotage;
177 Charlotte, NC). The samples were dissolved in 1 ml of hexane and transferred to the SPE
178 column, followed by a rinse with 1 ml of hexane to elute nonpolar compounds. Oxysterols
179 were eluted from the column with 4.5 ml of a 23:1 mixture of chloroform: methanol and dried
180 under nitrogen. Samples were resuspended in 50µl of warm (37°C) 90% methanol with 0.1%
181 DMSO, and placed in an ultrasonic bath for 5 min at 30°C. A standard curve was extracted
182 for 25-OHC (Sigma-Aldrich, H1015) and 7 α ,25-OHC (SML0541, Sigma-Aldrich) using the
183 above method. Dichloromethane, butylated hydroxytoluene (BHT) and hexane were
184 purchased from Sigma-Aldrich.

185
186 **Mass spectrometric quantitation of 25-OHC and 7 α ,25-OHC**

187 Samples were analysed on an AB Sciex QTRAP® 5500 (ABSCIEX, Redwood City, CA) mass
188 spectrometer coupled to a Shimadzu Nexera2 UHPLC. A Kinetex Pentafluorophenyl (PFP)
189 column (100 × 2.1mm, 1.7 μ M, 100⁰A, Phenomenex) was used for the separation of 25-OHC
190 and 7 α ,25-OHC from other oxysterols. Mobile phase used for separation were, A - 0.1%
191 formic acid with water and B - 100% acetonitrile with 0.1% formic acid. Five μ L of sample
192 were loaded at 0.5 mL/min and separated using linear gradient with increasing percentage
193 of acetonitrile. Samples were washed for 1.3 min after loading with 30% mobile phase B
194 followed by linear gradient of 30% - 70% over 9 min and 70% to 99% over 1 min. The column
195 was washed with 99% mobile phase B for 2 min followed by equilibration with 30% B 2 min
196 before next injection. Column oven and auto-sampler were operated at 50°C and 15°C,
197 respectively. Elution of analytes from the column was monitored in positive ion mode (ESI)
198 with multiple reaction monitoring on ABSciex QTRAP® mass spectrometer equipped with
199 Turbo spray ion source, which was operated at temp 550°C, ion spray voltage of 5500 V,
200 curtain gas (CUR) of 30 psi, ion source gas1 (GS1) of 65 psi and ion source gas 2 (GS2) of
201 50 psi. Quadrupole 1 and 3 were operated at unit mass resolution at all time during the
202 experiment. MRM pairs 385.3 > 367.3, 385 > 133, 385.3 > 147.1 were monitored for 25-OHC
203 and for 7 α ,25-OHC following MRM pairs were used 383.2 > 365.3, 383.2 > 147.3, 383.2 >
204 159.0. Deuterated 25-OHC (11099, Sapphire Bioscience, Redfern, Australia) and 7 α ,25-OHC
205 (700078P, Merck) were used as internal standards. Following MRM transitions were recoded
206 for internal standards 391.1 > 373.2, 391.1 > 133.1, 391.1 > 123.1 (25-OHC) and 407.2 > 389.0
207 (7 α ,25-OHC). De-clustering potential (DP), collision energy (CE), entrance (EP) and collision
208 cell exit potential (CXP) were optimised for each MRM pair to maximise the sensitivity. Data
209 was processed using AbSciex MultiQuant™ software (Version 3.0.3). Oxysterol
210 concentrations were subsequently normalized to the lung weights. High-performance liquid
211 chromatography (HPLC) grade methanol, acetonitrile and chloroform were purchased from
212 Merck.

213 **Cytokine quantification using ELISA**

214 Cytokines in lung homogenates were measured with DuoSet ELISA (IFN β (DY8234-05), IFN γ
215 (DY485), IFN λ (DY1789B), IL-6 (DY406), TNF α (DY410), IL-1 β (DY401), IL-10 (DY417) and
216 CCL2 (DY479), R&D systems) according to the manufacturer's protocol.

217 **Flow cytometry**

218 Lung lobes of IAV-infected mice digested in digestion buffer (Librase; Roche) and passed
219 through 40- μ m nylon mesh to obtain single cell suspensions. Red blood cells lysis performed

220 using BD Pharm Lyse (BD Biosciences, San Jose, CA). Cells were labelled with: Zombie
221 Green Fixable Viability kit (423111, Biolegend), PerCP-CD45 (30-F11), Brilliant Ultraviolet
222 395-CD3e (145-2C11, BD Biosciences), Brilliant Violet (BV) 786-CD4 (L3T4, BD
223 Biosciences), PE/Cyanine7-CD11b (M1/70), BV510-CD11c (N418), APC/Cyanine7-F4/80
224 (BM8), BV605-Ly6G (1A8, BD Bioscience), PE-B220 (RA3-6B2), BV421-I-A/I-E
225 (M5/114.15.2), APC-Siglec-F (CD170, S17007L, BD bioscience) before flow cytometric
226 analysis on the BD LSRFortessa X20. Post-acquisition analysis was performed using FlowJo
227 software (TreeStar).

228 **Immunohistochemistry**

229 Heat-induced epitope retrieval was performed using citrate buffer (pH 6, 95°C, 30 mins)
230 (BP327-1; Thermo Fisher Scientific). Sections were blocked for endogenous peroxidase
231 activity using 3% hydrogen peroxide (HL001-2.5L-P, Chem Supply, Adelaide, South
232 Australia), washed with tris-buffered saline (TBS; Bio-Rad) containing 0.05% polysorbate 20
233 (Tween-20; Sigma Aldrich; TBST) and blocked using background sniper (BS966, Biocare
234 Medical, Concord, CA) for 30 mins. Immunohistochemistry (IHC) was performed on
235 deparaffinized and rehydrated lung sections. Immunolabeling was performed with rabbit
236 antibodies against SARS-CoV-2 nucleocapsid protein antibody (1 hour at 25°C, 1:5000)
237 (40143-R040 Sino Biological), IBA1 (2 hours at 25°C 1:1000) (019-19741; NovaChem),
238 CH25H (4°C overnight 1:600) (BS-6480R, Bioss Antibodies), CYP7B1 (4°C overnight 1:1000)
239 (BS-5052R, Bioss Antibodies) and isotype control (rabbit IgG 31235, Thermo Fisher
240 Scientific) diluted in Da Vinci Green Diluent (PD900, Biocare Medical) followed by incubation
241 with horseradish peroxidase (HRP)-conjugated goat anti-rabbit Ig antibody (1:200) (ab6721,
242 Abcam). Isotype controls are shown in (**Figure S2**). Sections were washed with TBST before
243 applying chromogen detection, using diaminobenzidine (ab64238, DAB substrate kit Abcam,)
244 as per the manufacturer's instructions. Counterstaining was performed with Mayer's
245 hematoxylin (Sigma-Aldrich) before dehydrating the sections in a series of increasing ethanol
246 concentrations (70% to 100% ethanol). Sections were clarified with xylene, and mounted
247 using a xylene-based mounting medium (15-184-40, SHURMount Mounting Media, Fisher
248 scientific). Slides were scanned in an Olympus SLIDEVIEW VS200 using a 20x objective.
249 DAB-positive areas were quantified using ImageJ (<https://imagej.nih.gov/ij/>).

250 **Statistical analysis**

251 Data were analysed on GraphPad Prism software. Data were also assessed for normality
252 using Shapiro-Wilk test. Spearman rank correlation was used to analyse correlations. For two

253 group comparisons, parametric Student's two-tailed t test was used for normally distributed
254 data while nonparametric Mann-Whitney U test was used for skewed data that deviate from
255 normality.

256

257 **Results**

258 **IAV infection increases CH25H and CYP7B1 expression and oxysterol production in**
259 **the lung**

260 To investigate whether IAV infection induces the production of oxidized cholesterol, we
261 infected mice with IAV (**Figure 1B**) and determined the mRNA expression of oxysterol
262 producing enzymes in the lung. *Ch25h* and *Cyp7b1* mRNA was increased in the lungs of IAV-
263 infected mice compared to uninfected animals (**Figure 1C**). Similarly, CH25H and CYP7B1
264 protein expression was also increased, as demonstrated by immunohistochemical labelling
265 of lung sections with antibodies detecting CH25H and CYP7B1 protein (**Figure 1D,E**). The
266 induction of oxysterol producing enzymes was associated with increased concentrations of
267 the oxysterols 7 α ,25-OHC and 25-OHC in IAV-infected lungs at both 3 days post infection
268 (dpi) and 7 dpi (**Figure 1F, G**). In uninfected lungs, 7 α ,25-OHC was undetectable in most
269 samples tested. Consistent with the increase in oxysterols, *Gpr183* mRNA was increased at
270 3 dpi and 7 dpi (**Figure S3A**), suggesting increased recruitment of GPR183-expressing
271 immune cells to the lung upon infection. *Gpr183* expression was positively correlated with
272 *Ch25h* and *Cyp7b1* (**Figure S3B, C**).

273

274 ***Gpr183*^{-/-} mice have reduced macrophage infiltration into the lungs upon IAV infection**

275 To investigate whether oxysterol-mediated immune cell recruitment is dependent on
276 oxysterol-sensing GPR183, we performed experiments in mice genetically deficient in
277 *Gpr183* (*Gpr183*^{-/-}). *Gpr183*^{-/-} mice are viable and exhibit normal gross phenotype (25).
278 However, upon infection with IAV, *Gpr183*^{-/-} mice had lower IBA1⁺ macrophage numbers in
279 the lung at 3 dpi and 7 dpi compared to infected C57BL/6J controls (**Figure 2A**). *Gpr183*
280 expression was positively correlated with mRNA expression of the pro-inflammatory
281 cytokines *Il6*, *Tnf* and *Ccl2* in C57BL/6J mice (**Figure S4**) and reduced macrophage
282 infiltration in *Gpr183*^{-/-} mice was associated with reduced *Il6* and *Tnf*, but not *Ccl2* at 7 dpi
283 (**Figure S5**). Body weights and viral titers through the course of IAV infection were
284 comparable across the two genotypes (**Figure S6**). These results demonstrate that GPR183

285 is required for macrophage infiltration into the lung upon IAV infection and that lower
286 macrophage numbers are associated with reduced expression of pro-inflammatory cytokines.

287 **GPR183 inhibition reduces macrophage infiltration**

288 To investigate whether GPR183 is a putative therapeutic target to reduce inflammation, the
289 synthetic GPR183 antagonist NIBR189 (14, 21) was administered to C57BL/6J mice twice
290 daily starting from 24 h post-infection until the end of the experiment (**Figure 2B**). Like
291 *Gpr183*^{-/-} mice, C57BL/6J animals treated with NIBR189 had significantly reduced
292 macrophage infiltration into the lung both at 3 and 7 dpi as determined by IHC (**Figure 2C**).

293 In addition, flow cytometry analysis was performed on lung single cell suspensions from
294 C57BL/6J and *Gpr183*^{-/-} mice treated with NIBR189 and vehicle, respectively, using a
295 previously published gating strategy (26) (**Figure S7**). NIBR189-treated C57BL/6J mice and
296 *Gpr183*^{-/-} mice had lower percentages of macrophages (F480^{high}/CD11b⁺/Ly6G⁻/SigF⁻)
297 (**Figure 3A, B**) compared to vehicle-treated C57BL/6J animals after IAV infection. NIBR189
298 treatment did not change the percentages of other immune cell subsets in the lung, including
299 neutrophils (B220⁻/CD3⁻/Ly6G⁺/CD11b⁺) (**Figure 3A, C**), CD4⁺ T cells, CD8⁺ T cells, B cells,
300 DCs, and alveolar macrophages (**Figure S8**). Body weights and lung viral loads were not
301 affected by genotype or treatment (**Figure S9**).

302 Taken together our results demonstrate that the GPR183 antagonist NIBR189 significantly
303 reduced the infiltration of macrophages to the lung without affecting the recruitment of other
304 immune cell subsets to the site of infection.

305 **GPR183 inhibition reduces IAV-induced pro-inflammatory cytokine concentrations**

306 We next determined if the reduced macrophage infiltration mediated by the GPR183
307 antagonist NIBR189 results in reduced inflammatory cytokine production in the lung. At 3 dpi,
308 no significant differences in cytokine production were observed between treatment groups
309 (**Figure S10**). However, IAV-Infected C57BL/6J mice treated with NIBR189 had significantly
310 lower concentrations of IL-6, TNF and IFN β (**Figure 4A-D**) at 7 dpi. This was again
311 comparable to the phenotype of IAV-infected *Gpr183*^{-/-} mice, with NIBR189 treatment having
312 no additional effect in mice deficient in GPR183. In addition, no significant differences were
313 observed in IFN λ across the two timepoints (**Figure 4D and Figure S10**) demonstrating that
314 the GPR183 antagonist treatment does not negatively impact the production of type III IFNs
315 which are important for viral control in the lung (27). No differences between treatment groups
316 were observed at either timepoint for protein concentrations of IL-1 β , CCL2 or IFN γ between

317 treatment groups (**Figure S10 and S11**). Thus, GPR183 can be inhibited pharmacologically
318 to reduce proinflammatory cytokines upon severe IAV infection.

319 **GPR183 inhibition reduces SARS-CoV-2 infection severity**

320 Excessive macrophage infiltration and activation is a hallmark of severe COVID-19 (3, 28).
321 To evaluate whether the benefits of inhibiting GPR183 extend to SARS-CoV-2 infection, we
322 established a mouse-adapted SARS-CoV-2 strain by passaging the Beta variant of SARS-
323 CoV-2 (B.1.351) four times in C57BL/6J mice. This resulted in a viral stock that contained a
324 mutation in NSP5 and caused clinical signs in infected mice as indicated by body weight loss
325 (**Figure S1**). Consistent with the IAV infection results, mRNA expression of *Ch25h* and
326 *Cyp7b1* was significantly upregulated in the lungs of SARS-CoV-2 infected mice compared
327 to uninfected mice (**Figure 5A**). This was confirmed also at the protein level by IHC (**Figure**
328 **5B, C**). Further, 25-OHC and 7 α ,25-OHC concentrations in lung homogenates were
329 significantly increased at 2 dpi, returning to uninfected levels by 5 dpi by which time the
330 animals began to recover from the infection (**Figure 5D**). NIBR189 or vehicle was
331 administered to C57BL/6J or *Gpr183*^{-/-} mice twice daily from 24 h post-SARS-CoV-2 infection
332 until the end of the experiment (**Figure 6A**). NIBR189-treated C57BL/6J mice lost significantly
333 less weight and recovered faster compared to infected C57BL/6J mice receiving vehicle
334 (**Figure 6B and S12**). Similarly, *Gpr183*^{-/-} had less severe SARS-CoV-2 infection.
335 Collectively, these data demonstrate that oxysterols are produced in the lung upon SARS-
336 CoV-2 infection and inhibition of GPR183 significantly reduced the severity of SARS-CoV-2
337 infection.

338 **GPR183 inhibition reduces macrophage infiltration and inflammatory cytokine
339 expression in the lung of SARS-CoV-2 infected mice**

340 Next, we investigated whether the inhibition of GPR183 also decreases macrophage
341 infiltration and inflammatory cytokines in the lung. SARS-CoV-2-infected C57BL/6J mice
342 treated with NIBR189 had significantly reduced macrophage infiltration into the lung at 2 dpi
343 and 5 dpi (**Figure 6C**). NIBR189 treatment was also associated with reduced *Tnf*, *Il10* and
344 *Ifng* mRNA expression at 2 dpi (**Figure 7A-C**), as well as reduced *Tnf*, *Il1b* and *Il6* expression
345 at 5 dpi (**Figure 7D-F**). Early interferon responses were not affected by NIBR189 treatment
346 with comparable *Ifnb* and *Ifnl* expression at 2 dpi in C57BL/6J mice that received NIBR189
347 treatment versus vehicle (**Figure 8A, B**). Late interferon responses (5 dpi) were significantly
348 lower in NIBR-treated animals compared to controls (**Figure 8C, D**). No differences between
349 treatment groups were observed for mRNAs encoding *Ccl2*, *Il1b*, or *Il6* at 2 dpi as well as

350 those encoding *Ccl2*, *Il10* and *Ifng* at 5 dpi (**Figure S13**). These results demonstrate that
351 reduced macrophage infiltration in NIBR-treated mice was associated with reduced pro-
352 inflammatory cytokine expression in the lung, while the early antiviral IFN responses
353 remained unchanged. The mechanism(s) by which oxysterols attract macrophages to the
354 lung to produce pro-inflammatory cytokines are therefore conserved across viral infections.

355 **GPR183 inhibition reduces SARS-CoV-2 loads**

356 Finally, we investigated whether the reduced macrophage infiltration and inflammatory
357 cytokine profile in the lung of the NIBR189-treated mice is associated with altered viral loads.
358 Viral nucleocapsid protein (Np) expression was reduced in C57BL/6J mice treated with
359 NIBR189 compared to those administered vehicle at 2 dpi (**Figure 9A, B**). Np expression
360 was not detected at 5 dpi, when the animals recovered from the infection. However, at the
361 mRNA level, viral *Mpro* RNA loads in the lungs of NIBR189-treated mice were significantly
362 lower at 5 dpi (**Figure 9C**). In summary, we demonstrate here that GPR183 inhibition reduces
363 viral loads, macrophage infiltration and production of pro-inflammatory cytokines that are
364 typically associated with immunopathology in the lung (**Figure 10**).

365 **Discussion**

366 Here, we report that the oxysterols 25-OHC and 7 α ,25-OHC are produced in the lung upon
367 infection with either IAV or SARS-CoV-2 and attract monocytes-macrophages in a GPR183
368 dependent manner to the lung. Excessive macrophage infiltration and inflammation triggers
369 lung pathology and results in severe respiratory infection outcomes (1, 2, 29). Reduced
370 macrophage infiltration in *Gpr183*^{-/-} mice, as well as in C57BL/6J mice treated with the
371 GPR183 antagonist NIBR189, was associated with reduced inflammatory cytokine
372 production in the lungs of IAV and SARS-CoV-2 infected animals. Blocking GPR183 in
373 SARS-CoV-2-infected mice significantly improved SARS-CoV-2 infection severity and
374 attenuated viral loads. The antagonist had no impact on IAV viral loads and whether this is
375 due to pathogen-specific effects or due to more severe disease observed by increased weight
376 loss in the IAV model compared to the SARS-CoV-2 model, remains to be investigated.
377 However, macrophage infiltration and cytokine production was reduced in both viral models.

378 In non-human primates, influenza virus infection leads to infiltration of myeloid cells into the
379 lungs (30). Similarly, in several animal models of acute infection with SARS-CoV-2,
380 macrophages rapidly infiltrate the lungs (4-6). Patients with severe COVID-19 infection had
381 higher proportions of macrophages and neutrophils in BALF, with the macrophage phenotype
382 from deceased COVID-19 patients being more activated (28). This strongly implicates
383 macrophages as key cellular contributors to COVID-19-associated hyperinflammation. In
384 BALF from patients with severe COVID-19, the chemokines CCL2 and CCL7 that recruit
385 monocytes to the lung via the chemokine receptor CCR2 are also significantly enriched (31).
386 Historically, chemokines have been considered as the main drivers of immune cell migration
387 into the lung; however, our work here reveals that oxysterols have a non-redundant role in
388 macrophage infiltration. Similar to our observations in *Gpr183*^{-/-} mice, mice lacking the
389 chemokine receptor CCR2 have a significant delay in macrophage infiltration into the lung
390 (26). However, CCR2 is also required for T cell migration, therefore, animals lacking CCR2
391 also had delayed T cell infiltration, which correlated with significantly higher pulmonary viral
392 titers (32). Although GPR183 is expressed on T cells it is not essential for T cell migration
393 into the lung (33) and thus blocking GPR183 in our preclinical models did not negatively
394 impact the T cell compartment nor other immune cell subsets.

395 We recently showed in a murine model of *Mycobacterium tuberculosis* (Mtb) infection that
396 both GPR183 and CYP7B1, which produces the endogenous high affinity GPR183 agonist
397 7 α ,25-OHC, are required for rapid macrophage infiltration into the lung upon bacterial

398 infection (24). In the Mtb model, GPR183 was also required for infiltration of eosinophils into
399 the lung (18).

400 Reduced macrophage infiltration in both *Gpr183*^{-/-} mice and C57BL/6J mice treated with the
401 GPR183 antagonist NIBR189 was associated with reduced pro-inflammatory cytokine
402 production in the lung of both IAV and SARS-CoV-2 infected animals, likely due to lower
403 numbers of pro-inflammatory macrophages present in the tissue. However, we cannot
404 exclude a direct effect of the GPR183 antagonist on cytokine production in macrophages and
405 potentially other immune cell subsets like T cells. We previously showed that GPR183 is a
406 constitutively negative regulator of type I IFNs in primary human monocytes infected with Mtb
407 (34). *In vitro* activation of GPR183 with the agonist 7 α ,25-OHC reduced Mtb-induced *Ifnb*
408 mRNA levels, while the GPR183 antagonist GSK682753 significantly increased *Ifnb* mRNA
409 expression elicited by Mtb (34). This antagonist did not affect *Tnf* transcription in these *in vitro*
410 assays; however, it cannot be excluded that NIBR189 used in the experiments presented
411 here directly affects cytokine expression in macrophages or other immune cell subsets.

412 Irrespective of the exact mechanism, reduced pro-inflammatory cytokine production was
413 associated with reduced SARS-CoV-2 infection severity. Excessive production of
414 proinflammatory cytokines contributes to the immunopathology in COVID-19 patients with
415 severe disease (35). Therefore, lower pro-inflammatory cytokine production in animals
416 treated with NIBR189 can explain, at least in part, the better disease outcomes compared to
417 vehicle-treated animals. While cytokines can be detrimental to the host and contribute to the
418 development of cytokine storms (36), early type I and III IFNs are crucial in controlling viral
419 replication during IAV (37, 38) and SARS-CoV-2 infections (39, 40), whereas prolonged type
420 I IFN responses can be detrimental to the host (41). The GPR183 antagonist did not alter
421 early type I or III IFN responses in SARS-CoV-2-infected animals, suggesting that the anti-
422 viral response was not impaired by the treatment. However, antagonising GPR183 prevented
423 a prolonged IFN response, which was associated with more effective viral clearance
424 observed in NIBR189-treated animals.

425 While several oxysterols can have a direct anti-viral effect (12), it is not known whether
426 NIBR189 directly affects viral entry or replication. CH25H/25-OHC have been shown to inhibit
427 SARS-CoV-2 infection *in vitro* by blocking the virus-host cell membrane fusion (42, 43). It is
428 unlikely that NIBR189 directly affects viral entry and/or replication, given that it is structurally

429 very different from cholesterol and probably not able to disrupt the host cell membrane
430 composition typical for other anti-viral oxysterols.

431 We propose that GPR183, which belongs to the GPCR family, is a novel drug target for
432 severe COVID-19. GPCRs are popular targets because of their pharmacological tractability.
433 Indeed, 34% of all FDA approved drugs are directed against members of this receptor family,
434 with this accounting for global sales volumes of over 180 billion US dollars (44). In our SARS-
435 CoV-2 model the GPR183 antagonist demonstrated a dual benefit by not only reducing pro-
436 inflammatory cytokines without compromising early type I and type III IFN responses, but
437 also by reducing viral loads. Other immunosuppressive therapies used in severe COVID-19
438 like glucocorticoids can increase ACE2 expression which promotes viral entry and replication
439 (45, 46). Consistent with this, glucocorticoid use delays SARS-CoV-2 clearance (47).
440 Glucocorticoids can also affect antibody production. While it remains to be established
441 whether NIBR189 has a similar effect, short term use of a GPR183 antagonist during the
442 acute viral infection is unlikely to negatively impact antibody responses. Currently available
443 antiviral treatments are effective, but mutations in SARS-CoV-2 conferring resistance to new
444 antivirals are already emerging (48). Therefore, adjunct host-directed therapy with a GPR183
445 antagonist together with conventional antivirals may increase treatment efficacy. Since a
446 GPR183 antagonist targets the host and not the virus it is not anticipated that viruses will
447 develop resistance against host directed therapy (49). Further, a GPR183 antagonist-based
448 therapy can also be immediately effective against newly emerging SARS-CoV-2 variants
449 without further adaption.

450 In summary, we provide the first preclinical evidence of GPR183 as a novel host target for
451 therapeutic intervention to reduce macrophage-mediated hyperinflammation, SARS-CoV-2
452 loads and disease severity in COVID-19.

453 **Acknowledgements**

454 This study was supported by grants to KR from the Mater Foundation, the Australian
455 Respiratory Council, Diabetes Australia, and the Australian Infectious Diseases Research
456 Centre. SB was supported by an early career seed grant from the Mater Foundation. The
457 Translational Research Institute is supported by a grant from the Australian Government. We
458 thank A/Prof Sumaira Hasnain for sharing antibodies used in this study. We thank the
459 Queensland Health Forensic and Scientific Services, Queensland Department of Health, for
460 providing SARS-CoV-2 isolate. We acknowledge the technical assistance of the team that
461 operates and maintains the Australian Galaxy service (<https://usegalaxy.org.au/>). The Danish
462 Council for Independent Research I Medical Sciences supported MMR. MJS is supported by
463 a National Health and Medical Research Council of Australia Investigator grant
464 (APP1194406). KRS is funded by the NHMRC Investigator Grant (2007919) and is consultant
465 for Sanofi, Roche and NovoNordisk. MMR is co-founder of Antag Therapeutics and of
466 Synkline. The opinions and data presented in this manuscript are of the authors and are
467 independent of these relationships. Other authors declare no competing interests. We thank
468 Profs David Hume, Jean-Pierre Levesque and Maher Gandhi for critical review of the
469 manuscript.

470 **Author contributions**

471 Conceptualization: CXF, SB, MJS, KRS, MMR, KR Methodology: KYC, HBO, BJA, BM, SR
472 Investigation: CXF, SB, KYC, MDN, HBO, BJA, BM, SR, RW, LB, JES, RP, AK Writing-
473 original draft: CXF, SB, KR Writing-review and editing: all authors. Funding acquisition: SB,
474 KRS, MMR, KR.

475

476

477

478

479

480

481

482 **References**

483 1. Flerlage T, Boyd DF, Meliopoulos V, Thomas PG, Schultz-Cherry S. 2021. Influenza
484 virus and SARS-CoV-2: pathogenesis and host responses in the respiratory tract. *Nat*
485 *Rev Microbiol* 19:425-441.

486 2. Short KR, Kroeze E, Fouchier RAM, Kuiken T. 2014. Pathogenesis of influenza-
487 induced acute respiratory distress syndrome. *Lancet Infect Dis* 14:57-69.

488 3. Chen ST, Park MD, Del Valle DM, Buckup M, Tabachnikova A, Simons NW, Mouskas
489 K, Lee B, Geanon D, D'Souza D, Dawson T, Marvin R, Nie K, Thompson RC, Zhao Z,
490 LeBerichel J, Chang C, Jamal H, Chaddha U, Mathews K, Acquah S, Brown SA, Reiss
491 M, Harkin T, Feldmann M, Powell CA, Hook JL, Kim-Schulze S, Rahman AH, Brown
492 BD, Mount Sinai C-BT, Beckmann ND, Gnjatic S, Kenigsberg E, Charney AW, Merad
493 M. 2022. Shift of lung macrophage composition is associated with COVID-19 disease
494 severity and recovery. *bioRxiv* doi:10.1101/2022.01.11.475918.

495 4. Speranza E, Williamson BN, Feldmann F, Sturdevant GL, Perez-Perez L, Meade-
496 White K, Smith BJ, Lovaglio J, Martens C, Munster VJ, Okumura A, Shaia C,
497 Feldmann H, Best SM, de Wit E. 2021. Single-cell RNA sequencing reveals SARS-
498 CoV-2 infection dynamics in lungs of African green monkeys. *Sci Transl Med* 13.

499 5. Lee JS, Koh JY, Yi K, Kim YI, Park SJ, Kim EH, Kim SM, Park SH, Ju YS, Choi YK,
500 Park SH. 2021. Single-cell transcriptome of bronchoalveolar lavage fluid reveals
501 sequential change of macrophages during SARS-CoV-2 infection in ferrets. *Nat*
502 *Commun* 12:4567.

503 6. Singh DK, Aladyeva E, Das S, Singh B, Esaulova E, Swain A, Ahmed M, Cole J,
504 Moodley C, Mehra S, Schlesinger LS, Artyomov MN, Khader SA, Kaushal D. 2022.
505 Myeloid cell interferon responses correlate with clearance of SARS-CoV-2. *Nat*
506 *Commun* 13:679.

507 7. Mirchandani AS, Jenkins SJ, Bain CC, Sanchez-Garcia MA, Lawson H, Coelho P,
508 Murphy F, Griffith DM, Zhang A, Morrison T, Ly T, Arienti S, Sadiku P, Watts ER,
509 Dickinson RS, Reyes L, Cooper G, Clark S, Lewis D, Kelly V, Spanos C, Musgrave
510 KM, Delaney L, Harper I, Scott J, Parkinson NJ, Rostron AJ, Baillie JK, Clohisey S,
511 Pridans C, Campana L, Lewis PS, Simpson AJ, Dockrell DH, Schwarze J, Hirani N,
512 Ratcliffe PJ, Pugh CW, Kranc K, Forbes SJ, Whyte MKB, Walmsley SR. 2022. Hypoxia
513 shapes the immune landscape in lung injury and promotes the persistence of
514 inflammation. *Nat Immunol* 23:927-939.

515 8. Shen ZJ, Hu J, Kashi VP, Kelly EA, Denlinger LC, Lutchman K, McDonald JG, Jarjour
516 NN, Malter JS. 2017. Epstein-Barr Virus-induced Gene 2 Mediates Allergen-induced
517 Leukocyte Migration into Airways. *Am J Respir Crit Care Med* 195:1576-1585.

518 9. Jia J, Conlon TM, Sarker RS, Tasdemir D, Smirnova NF, Srivastava B, Verleden SE,
519 Gunes G, Wu X, Prehn C, Gao J, Heinzelmann K, Lintelmann J, Irmler M, Pfeiffer S,
520 Schloter M, Zimmermann R, Hrabe de Angelis M, Beckers J, Adamski J, Bayram H,
521 Eickelberg O, Yildirim AO. 2018. Cholesterol metabolism promotes B-cell positioning
522 during immune pathogenesis of chronic obstructive pulmonary disease. *EMBO Mol*
523 *Med* 10.

524 10. Sugiura H, Koarai A, Ichikawa T, Minakata Y, Matsunaga K, Hirano T, Akamatsu K,
525 Yanagisawa S, Furusawa M, Uno Y, Yamasaki M, Satomi Y, Ichinose M. 2012.
526 Increased 25-hydroxycholesterol concentrations in the lungs of patients with chronic
527 obstructive pulmonary disease. *Respirology* 17:533-40.

528 11. Reinmuth L, Hsiao CC, Hamann J, Rosenkilde M, Mackrill J. 2021. Multiple Targets
529 for Oxysterols in Their Regulation of the Immune System. *Cells* 10.

530 12. Foo CX, Bartlett S, Ronacher K. 2022. Oxysterols in the Immune Response to
531 Bacterial and Viral Infections. *Cells* 11.

532 13. Mutemberezi V, Guillemot-Legrus O, Muccioli GG. 2016. Oxysterols: From cholesterol
533 metabolites to key mediators. *Prog Lipid Res* 64:152-169.

534 14. Hannedouche S, Zhang J, Yi T, Shen W, Nguyen D, Pereira JP, Guerini D,
535 Baumgarten BU, Roggo S, Wen B, Knochenmuss R, Noel S, Gessier F, Kelly LM,
536 Vanek M, Laurent S, Preuss I, Miault C, Christen I, Karuna R, Li W, Koo DI, Suply T,
537 Schmedt C, Peters EC, Falchetto R, Katopodis A, Spanka C, Roy MO, Detheux M,
538 Chen YA, Schultz PG, Cho CY, Seuwen K, Cyster JG, Sailer AW. 2011. Oxysterols
539 direct immune cell migration via EBI2. *Nature* 475:524-7.

540 15. Liu C, Yang XV, Wu J, Kuei C, Mani NS, Zhang L, Yu J, Sutton SW, Qin N, Banie H,
541 Karlsson L, Sun S, Loberberg TW. 2011. Oxysterols direct B-cell migration through
542 EBI2. *Nature* 475:519-23.

543 16. Spann NJ, Glass CK. 2013. Sterols and oxysterols in immune cell function. *Nat
544 Immunol* 14:893-900.

545 17. Emgard J, Kammoun H, Garcia-Cassani B, Chesne J, Parigi SM, Jacob JM, Cheng
546 HW, Evren E, Das S, Czarnecki P, Sleiers N, Melo-Gonzalez F, Kvedaraite E,
547 Svensson M, Scandella E, Hepworth MR, Huber S, Ludewig B, Peduto L, Villalblanca
548 EJ, Veiga-Fernandes H, Pereira JP, Flavell RA, Willinger T. 2018. Oxysterol Sensing
549 through the Receptor GPR183 Promotes the Lymphoid-Tissue-Inducing Function of
550 Innate Lymphoid Cells and Colonic Inflammation. *Immunity* 48:120-132 e8.

551 18. Bohrer AC, Castro E, Tocheny CE, Assmann M, Schwarz B, Bohrnsen E, Makiya MA,
552 Legrand F, Hilligan KL, Baker PJ, Torres-Juarez F, Hu Z, Ma H, Wang L, Niu L, Zilu
553 W, Lee SH, Kamenyeva O, Program TI, Kauffman KD, Donato M, Sher A, Barber DL,
554 Via LE, Scriba TJ, Khatri P, Song Y, Wong K-W, Bosio CM, Klion AD, Mayer-Barber
555 KD. 2022. Rapid GPR183-mediated recruitment of eosinophils to the lung after
556 Mycobacterium tuberculosis infection. doi:10.1101/2022.02.18.480919
557 %J bioRxiv:2022.02.18.480919.

558 19. Rutkowska A, O'Sullivan SA, Christen I, Zhang J, Sailer AW, Dev KK. 2016. The EBI2
559 signalling pathway plays a role in cellular crosstalk between astrocytes and
560 macrophages. *Sci Rep* 6:25520.

561 20. Preuss I, Ludwig MG, Baumgarten B, Bassilana F, Gessier F, Seuwen K, Sailer AW.
562 2014. Transcriptional regulation and functional characterization of the oxysterol/EBI2
563 system in primary human macrophages. *Biochem Biophys Res Commun* 446:663-8.

564 21. Gessier F, Preuss I, Yin H, Rosenkilde MM, Laurent S, Endres R, Chen YA, Marsilje
565 TH, Seuwen K, Nguyen DG, Sailer AW. 2014. Identification and characterization of
566 small molecule modulators of the Epstein-Barr virus-induced gene 2 (EBI2) receptor.
567 *J Med Chem* 57:3358-68.

568 22. Short KR, Diavatopoulos DA, Reading PC, Brown LE, Rogers KL, Strugnell RA,
569 Wijburg OL. 2011. Using bioluminescent imaging to investigate synergism between
570 *Streptococcus pneumoniae* and influenza A virus in infant mice. *J Vis Exp*
571 doi:10.3791/2357.

572 23. Schimmel L, Chew KY, Stocks CJ, Yordanov TE, Essebier P, Kulasinghe A, Monkman
573 J, Dos Santos Miggioro AFR, Cooper C, de Noronha L, Schroder K, Lagendijk AK,
574 Labzin LI, Short KR, Gordon EJ. 2021. Endothelial cells are not productively infected
575 by SARS-CoV-2. *Clin Transl Immunology* 10:e1350.

576 24. Ngo MD, Bartlett S, Bielefeldt-Ohmann H, Foo CX, Sinha R, Arachige BJ, Reed S,
577 Mandrup-Poulsen T, Rosenkilde MM, Ronacher K. 2022. A blunted GPR183/oxysterol
578 axis during dysglycemia results in delayed recruitment of macrophages to the lung
579 during *M. tuberculosis* infection. *J Infect Dis* doi:10.1093/infdis/jiac102.

580 25. Pereira JP, Kelly LM, Xu Y, Cyster JG. 2009. EBI2 mediates B cell segregation
581 between the outer and centre follicle. *Nature* 460:1122-6.

582 26. Poczobutt JM, Gijon M, Amin J, Hanson D, Li H, Walker D, Weiser-Evans M, Lu X,
583 Murphy RC, Nemenoff RA. 2013. Eicosanoid profiling in an orthotopic model of lung
584 cancer progression by mass spectrometry demonstrates selective production of
585 leukotrienes by inflammatory cells of the microenvironment. *PLoS One* 8:e79633.

586 27. Zhou JH, Wang YN, Chang QY, Ma P, Hu Y, Cao X. 2018. Type III Interferons in Viral
587 Infection and Antiviral Immunity. *Cell Physiol Biochem* 51:173-185.

588 28. Liao M, Liu Y, Yuan J, Wen Y, Xu G, Zhao J, Cheng L, Li J, Wang X, Wang F, Liu L,
589 Amit I, Zhang S, Zhang Z. 2020. Single-cell landscape of bronchoalveolar immune
590 cells in patients with COVID-19. *Nat Med* 26:842-844.

591 29. Baskin CR, Bielefeldt-Ohmann H, Tumpey TM, Sabourin PJ, Long JP, Garcia-Sastre
592 A, Tolnay AE, Albrecht R, Pyles JA, Olson PH, Aicher LD, Rosenzweig ER, Murali-
593 Krishna K, Clark EA, Kotur MS, Fornek JL, Proll S, Palermo RE, Sabourin CL, Katze
594 MG. 2009. Early and sustained innate immune response defines pathology and death
595 in nonhuman primates infected by highly pathogenic influenza virus. *Proc Natl Acad
596 Sci U S A* 106:3455-60.

597 30. Corry J, Kettenburg G, Upadhyay AA, Wallace M, Marti MM, Wonderlich ER, Bissel
598 SJ, Goss K, Sturgeon TJ, Watkins SC, Reed DS, Bosinger SE, Barratt-Boyes SM.
599 2022. Infiltration of inflammatory macrophages and neutrophils and widespread
600 pyroptosis in lung drive influenza lethality in nonhuman primates. *PLoS Pathog*
601 18:e1010395.

602 31. Zhou Z, Ren L, Zhang L, Zhong J, Xiao Y, Jia Z, Guo L, Yang J, Wang C, Jiang S,
603 Yang D, Zhang G, Li H, Chen F, Xu Y, Chen M, Gao Z, Yang J, Dong J, Liu B, Zhang
604 X, Wang W, He K, Jin Q, Li M, Wang J. 2020. Heightened Innate Immune Responses
605 in the Respiratory Tract of COVID-19 Patients. *Cell Host Microbe* 27:883-890 e2.

606 32. Dawson TC, Beck MA, Kuziel WA, Henderson F, Maeda N. 2000. Contrasting effects
607 of CCR5 and CCR2 deficiency in the pulmonary inflammatory response to influenza A
608 virus. *Am J Pathol* 156:1951-9.

609 33. Hoft SG, Sallin MA, Kauffman KD, Sakai S, Ganusov VV, Barber DL. 2019. The Rate
610 of CD4 T Cell Entry into the Lungs during *Mycobacterium tuberculosis* Infection Is
611 Determined by Partial and Opposing Effects of Multiple Chemokine Receptors. *Infect
612 Immun* 87.

613 34. Bartlett S, Gemiarto AT, Ngo MD, Sajir H, Hailu S, Sinha R, Foo CX, Kleynhans L,
614 Tshivhula H, Webber T, Bielefeldt-Ohmann H, West NP, Hiemstra AM, MacDonald
615 CE, Christensen LVV, Schlesinger LS, Walzl G, Rosenkilde MM, Mandrup-Poulsen T,
616 Ronacher K. 2020. GPR183 Regulates Interferons, Autophagy, and Bacterial Growth
617 During *Mycobacterium tuberculosis* Infection and Is Associated With TB Disease
618 Severity. *Front Immunol* 11:601534.

619 35. Del Valle DM, Kim-Schulze S, Huang HH, Beckmann ND, Nirenberg S, Wang B, Lavin
620 Y, Swartz TH, Madduri D, Stock A, Marron TU, Xie H, Patel M, Tuballes K, Van
621 Oekelen O, Rahman A, Kovatch P, Aberg JA, Schadt E, Jagannath S, Mazumdar M,
622 Charney AW, Firpo-Betancourt A, Mendum DR, Jhang J, Reich D, Sigel K, Cordon-
623 Cardo C, Feldmann M, Parekh S, Merad M, Gnjatic S. 2020. An inflammatory cytokine
624 signature predicts COVID-19 severity and survival. *Nat Med* 26:1636-1643.

625 36. Diamond MS, Kanneganti TD. 2022. Innate immunity: the first line of defense against
626 SARS-CoV-2. *Nat Immunol* 23:165-176.

627 37. Stanifer ML, Guo C, Doldan P, Boulant S. 2020. Importance of Type I and III
628 Interferons at Respiratory and Intestinal Barrier Surfaces. *Front Immunol* 11:608645.

629 38. Galani IE, Triantafyllia V, Eleminiadou EE, Koltsida O, Stavropoulos A, Manioudaki M,
630 Thanos D, Doyle SE, Kotenko SV, Thanopoulou K, Andreakos E. 2017. Interferon-
631 lambda Mediates Non-redundant Front-Line Antiviral Protection against Influenza
632 Virus Infection without Compromising Host Fitness. *Immunity* 46:875-890 e6.

633 39. Lokugamage KG, Hage A, de Vries M, Valero-Jimenez AM, Schindewolf C, Dittmann
634 M, Rajsbaum R, Menachery VD. 2020. Type I interferon susceptibility distinguishes
635 SARS-CoV-2 from SARS-CoV. *bioRxiv* doi:10.1101/2020.03.07.982264.

636 40. Vanderheiden A, Ralfs P, Chirkova T, Upadhyay AA, Zimmerman MG, Bedoya S,
637 Aoued H, Tharp GM, Pellegrini KL, Manfredi C, Sorscher E, Mainou B, Lobby JL,
638 Kohlmeier JE, Lowen AC, Shi PY, Menachery VD, Anderson LJ, Grakoui A, Bosinger
639 SE, Suthar MS. 2020. Type I and Type III Interferons Restrict SARS-CoV-2 Infection
640 of Human Airway Epithelial Cultures. *J Virol* 94.

641 41. Cameron MJ, Ran L, Xu L, Danesh A, Bermejo-Martin JF, Cameron CM, Muller MP,
642 Gold WL, Richardson SE, Poutanen SM, Willey BM, DeVries ME, Fang Y, Seneviratne
643 C, Bosinger SE, Persad D, Wilkinson P, Greller LD, Somogyi R, Humar A, Keshavjee
644 S, Louie M, Loeb MB, Brunton J, McGeer AJ, Canadian SRN, Kelvin DJ. 2007.
645 Interferon-mediated immunopathological events are associated with atypical innate
646 and adaptive immune responses in patients with severe acute respiratory syndrome.
647 *J Virol* 81:8692-706.

648 42. Wang S, Li W, Hui H, Tiwari SK, Zhang Q, Croker BA, Rawlings S, Smith D, Carlin
649 AF, Rana TM. 2020. Cholesterol 25-Hydroxylase inhibits SARS-CoV-2 and other
650 coronaviruses by depleting membrane cholesterol. *EMBO J* 39:e106057.

651 43. Zang R, Case JB, Yutuc E, Ma X, Shen S, Gomez Castro MF, Liu Z, Zeng Q, Zhao H,
652 Son J, Rothlauf PW, Kreutzberger AJB, Hou G, Zhang H, Bose S, Wang X, Vahey
653 MD, Mani K, Griffiths WJ, Kirchhausen T, Fremont DH, Guo H, Diwan A, Wang Y,
654 Diamond MS, Whelan SPJ, Ding S. 2020. Cholesterol 25-hydroxylase suppresses
655 SARS-CoV-2 replication by blocking membrane fusion. *Proc Natl Acad Sci U S A*
656 117:32105-32113.

657 44. Hauser AS, Chavali S, Masuho I, Jahn LJ, Martemyanov KA, Gloriam DE, Babu MM.
658 2018. Pharmacogenomics of GPCR Drug Targets. *Cell* 172:41-54 e19.

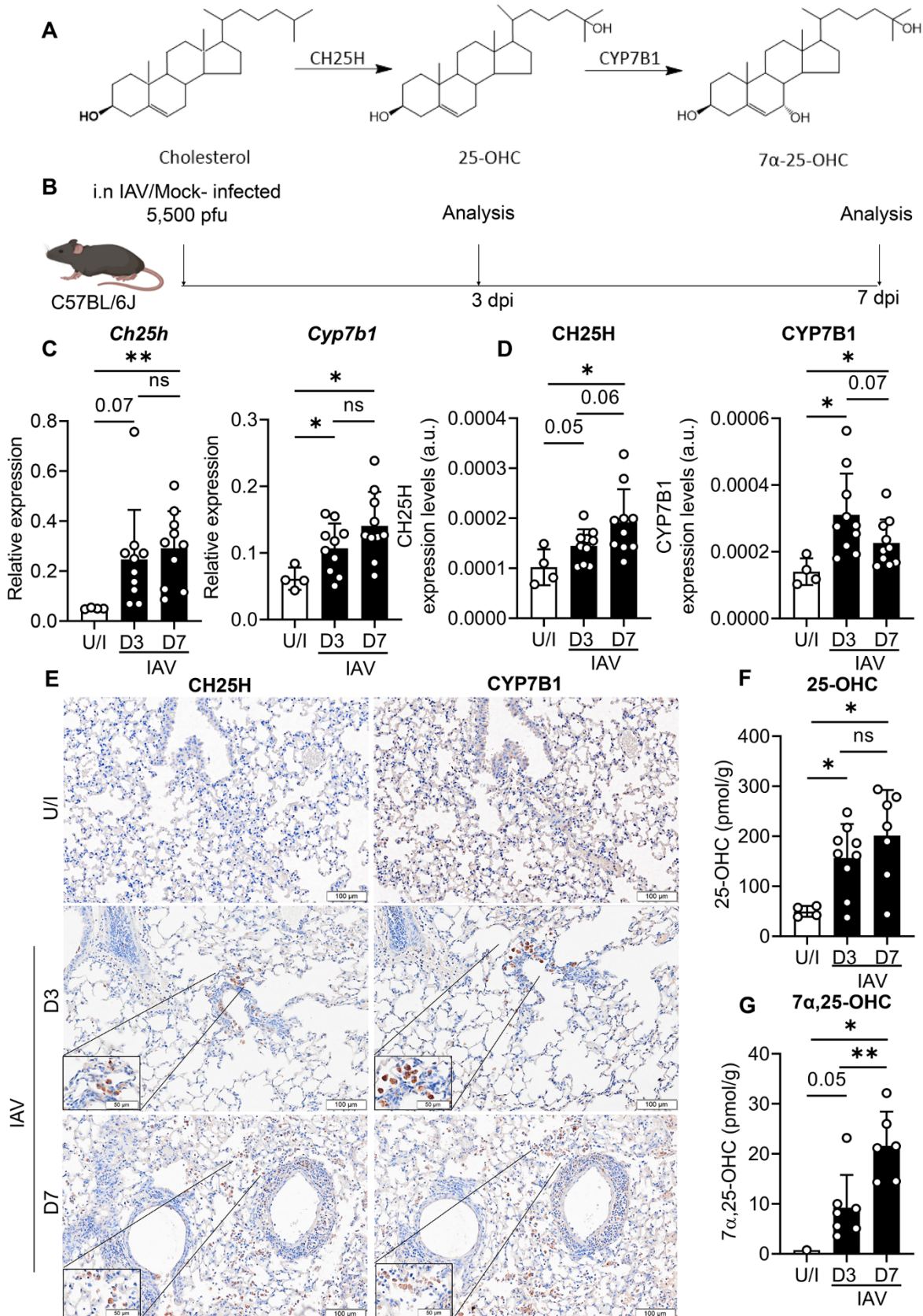
659 45. Sinha S, Cheng K, Schaffer AA, Aldape K, Schiff E, Ruppin E. 2020. In vitro and in
660 vivo identification of clinically approved drugs that modify ACE2 expression. *Mol Syst*
661 *Biol* 16:e9628.

662 46. Saheb Sharif-Askari N, Saheb Sharif-Askari F, Alabed M, Tayoun AA, Loney T, Uddin
663 M, Senok A, Al Hejaly S, Hamoudi R, Kashour T, Alsheikh-Ali A, Hamid Q, Halwani R.
664 2020. Effect of Common Medications on the Expression of SARS-CoV-2 Entry
665 Receptors in Kidney Tissue. *Clin Transl Sci* 13:1048-1054.

666 47. Li J, Liao X, Zhou Y, Wang L, Yang H, Zhang W, Zhang Z, Kang Y. 2021. Association
667 between glucocorticoids treatment and viral clearance delay in patients with COVID-
668 19: a systematic review and meta-analysis. *BMC Infect Dis* 21:1063.

669 48. Gandhi S, Klein J, Robertson AJ, Pena-Hernandez MA, Lin MJ, Roychoudhury P, Lu
670 P, Fournier J, Ferguson D, Mohamed Bakhsh SAK, Catherine Muenker M,
671 Srivathsan A, Wunder EA, Jr., Kerantzas N, Wang W, Lindenbach B, Pyle A, Wilen
672 CB, Ogbuagu O, Greninger AL, Iwasaki A, Schulz WL, Ko AI. 2022. De novo
673 emergence of a remdesivir resistance mutation during treatment of persistent SARS-
674 CoV-2 infection in an immunocompromised patient: a case report. *Nat Commun*
675 13:1547.

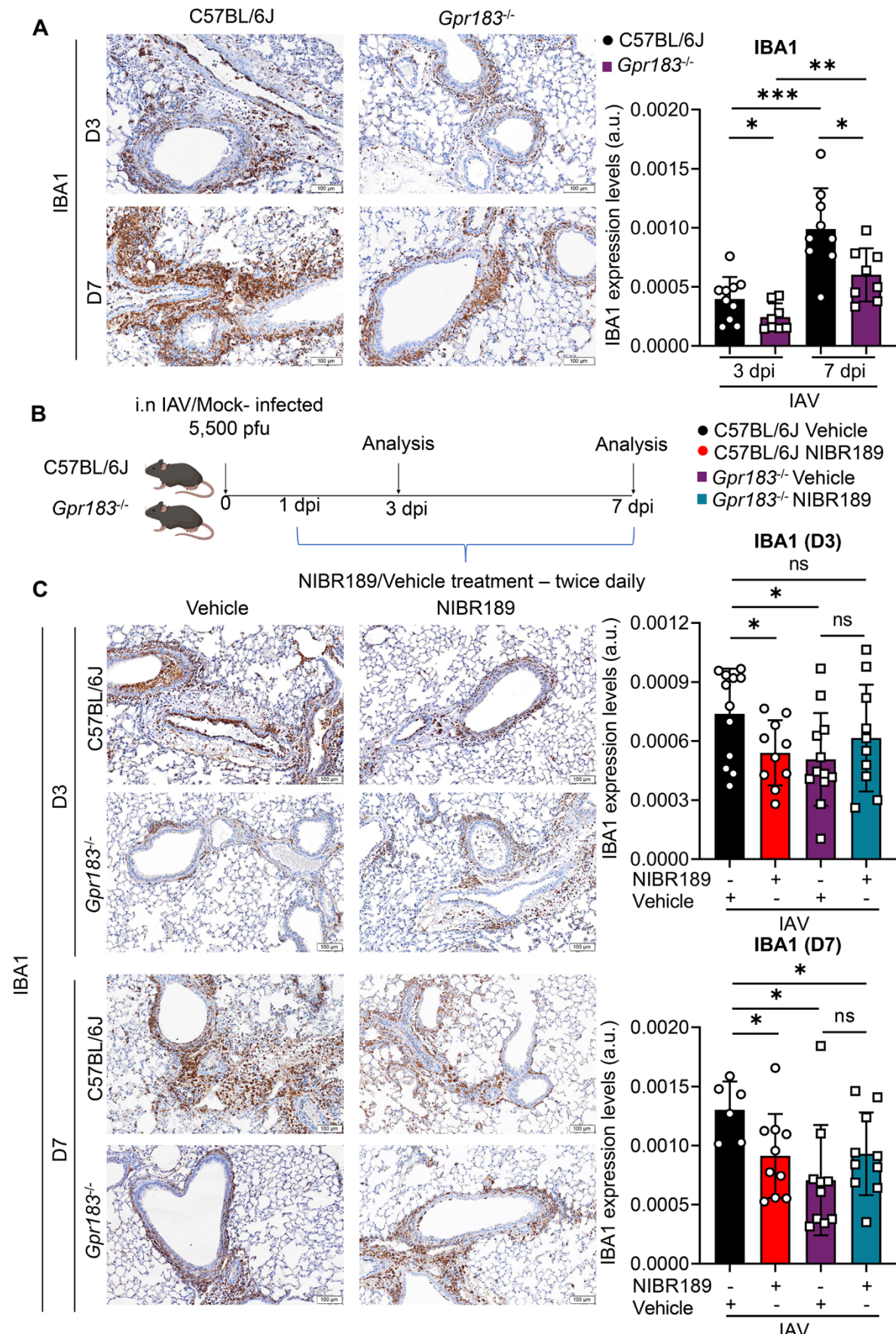
676 49. Wallis RS, O'Garra A, Sher A, Wack A. 2022. Host-directed immunotherapy of viral
677 and bacterial infections: past, present and future. *Nat Rev Immunol*
678 doi:10.1038/s41577-022-00734-z.



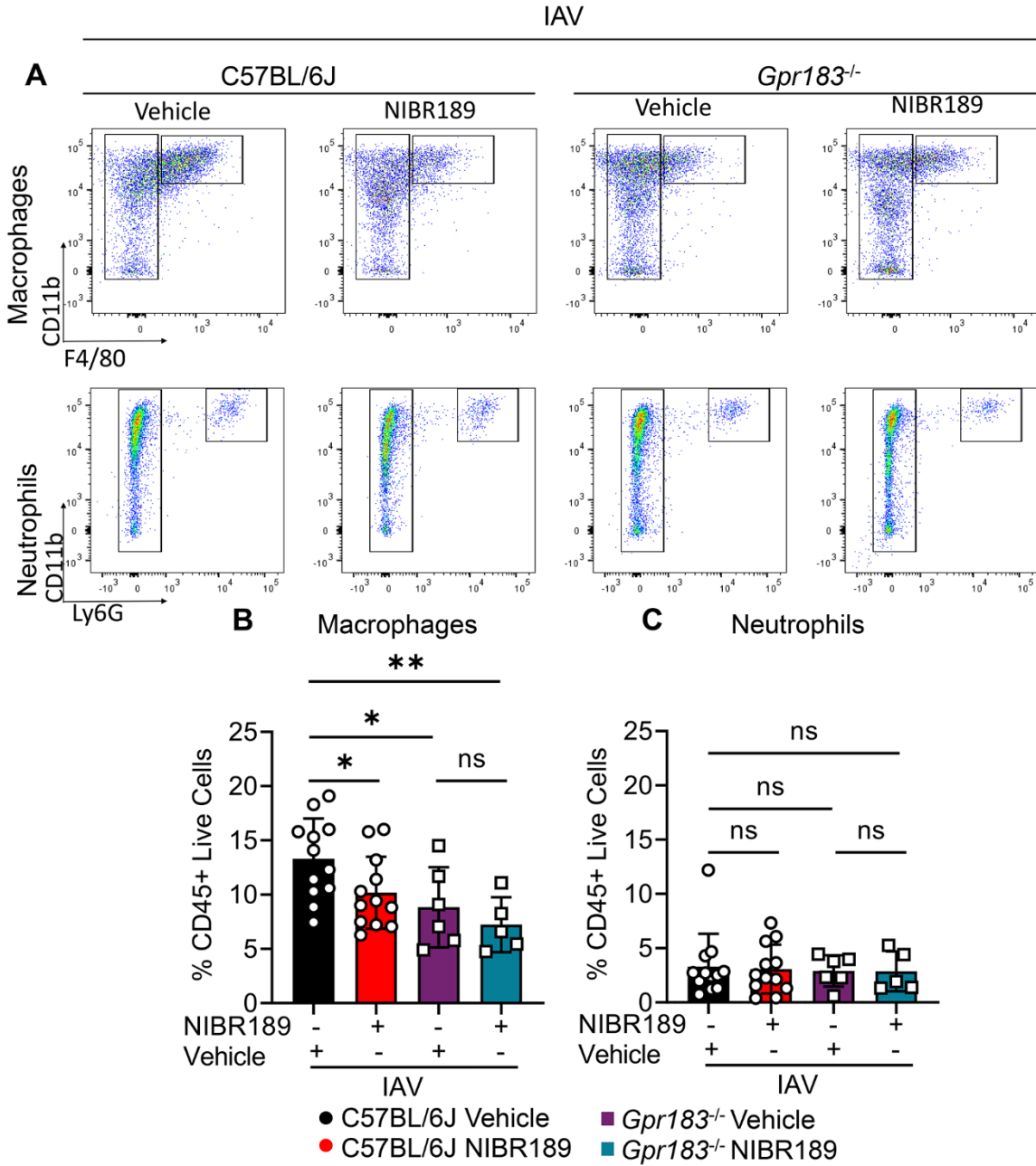
681 **Figure 1. IAV infection leads to upregulation of CH25H and CYP7B1 expression in the**
682 **lung and production of the oxysterols 25-OHC and 7 α ,25-OHC**

683 **A)** The biosynthetic pathway of 25-OHC and 7 α ,25-OHC. **B)** Experimental design. C57BL/6J
684 mice were infected intranasally with 5,500 PFU of A/Auckland/01/09 and mRNA expression
685 of **C)** *Ch25h* and *Cyp7b1* were measured by qRT-PCR at 3 dpi and 7 dpi normalized to *Hprt*.
686 **D)** Quantitative analysis of CH25H and CYP7B1 protein labelling by IHC. **E)** Representative
687 IHC images of CH25H and CYP7B1 in lung sections of uninfected or IAV-infected mice.
688 Concentrations of **F)** 25-OHC and **G)** 7 α ,25-OHC in the lungs at 3 dpi and 7 dpi expressed
689 in pmol per gram lung tissue. Data are presented as mean \pm SD of n=4 uninfected and n=6-
690 10 infected mice per timepoint. Scale Bar = 100 μ m; dpi = days post-infection; U/I = mock
691 infected; ns., not significant; *, P < 0.05; **, P <0.01 indicate significant differences.

692



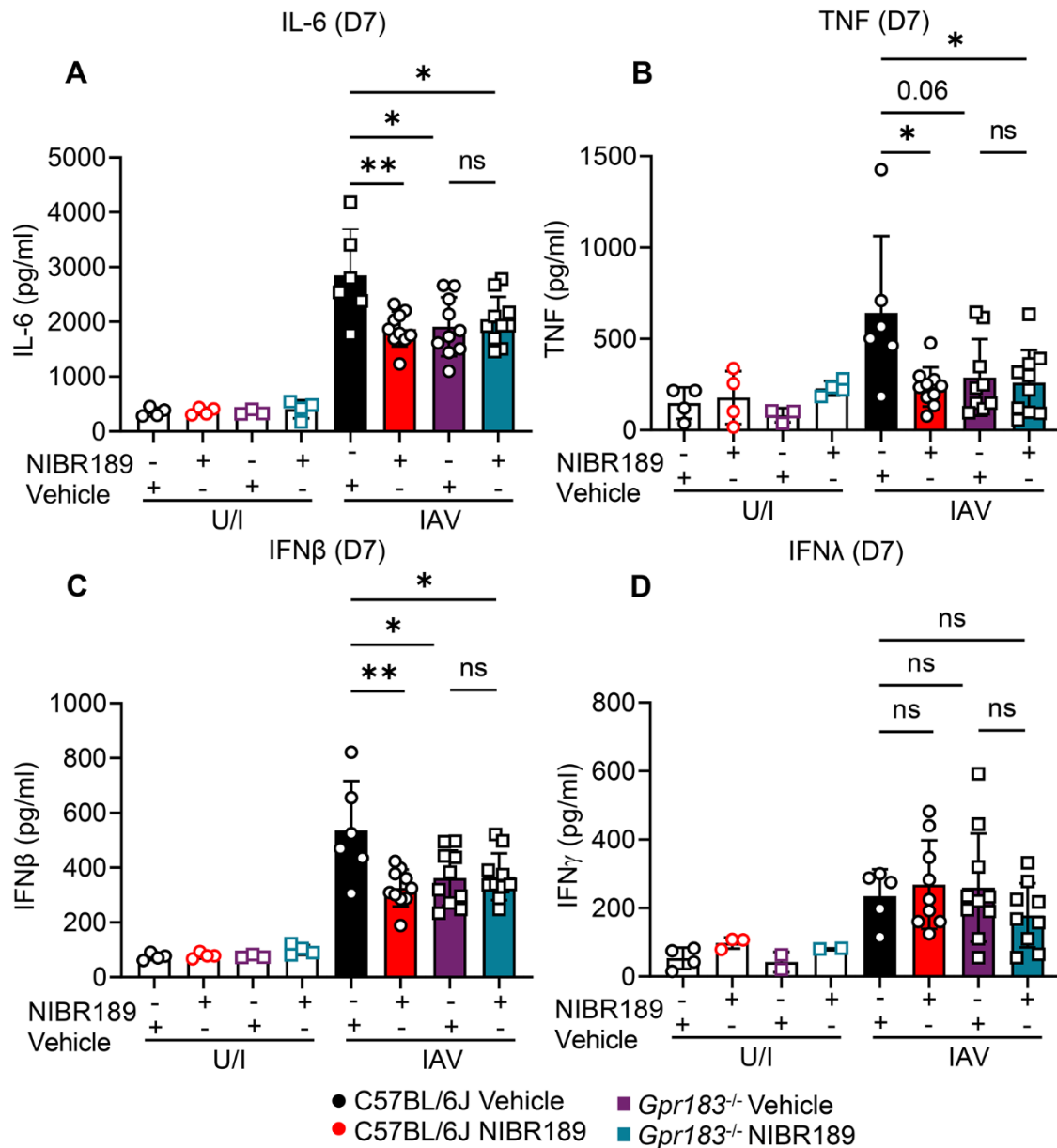
694 **Figure 2. Deletion of the *Gpr183* gene or administration of a GPR183 antagonist**
695 **reduces macrophage infiltration in IAV-infected lungs.** C57BL/6J and *Gpr183*^{-/-} mice
696 were infected intranasally with 5,500 PFU of A/Auckland/01/09. **A)** Representative IHC
697 images of IBA1 in lung sections of IAV-infected C57BL/6J and *Gpr183*^{-/-} mice. Quantitative
698 analysis of IBA1 staining. **B)** Experimental design; C57BL/6J mice and *Gpr183*^{-/-} mice were
699 infected intranasally with 5,500 PFU of A/Auckland/01/09. Mice were subsequently treated
700 orally with 7.6 mg/kg NIBR189 or vehicle control twice daily from 1 dpi until the end of the
701 experiment. **C)** Representative IHC images of IBA1 in lung sections of C57BL/6J and *Gpr183*
702 ^{-/-} mice with the respective treatment groups at 3dpi and 7dpi. Quantitative analysis of IBA1
703 staining. Data are presented as mean ± SD of n = 6-12 infected mice per genotype and
704 timepoint. dpi = days post-infection; Scale Bar = 100µm; U/I = mock infected ns = not
705 significant; *, P < 0.05; **, P < 0.01; ***, P < 0.001 indicate significant differences



706

707 **Figure 3. The GPR183 antagonist NIBR189 reduces macrophage infiltration and**
708 **inflammatory cytokine production.** C57BL/6J and *Gpr183*^{-/-} mice were infected intranasally
709 with 5,500 PFU of A/Auckland/01/09. Mice were subsequently treated orally with 7.6 mg/kg
710 NIBR189 or vehicle control twice daily from 1 dpi until the end of the experiment. **A)**
711 Frequency of infiltrating macrophages (F480^{high}/CD11b⁺/Ly6G⁻/SigF⁻) and neutrophils (B220⁻
712 CD3⁻Ly6G⁺) was determined by flow cytometry relative to total viable CD45⁺ immune cells 3
713 dpi. Graphs depicting the frequency of **B)** macrophages and **C)** neutrophils. Data are
714 presented as mean \pm SD of n=5-12 infected mice per genotype and timepoint. dpi = days

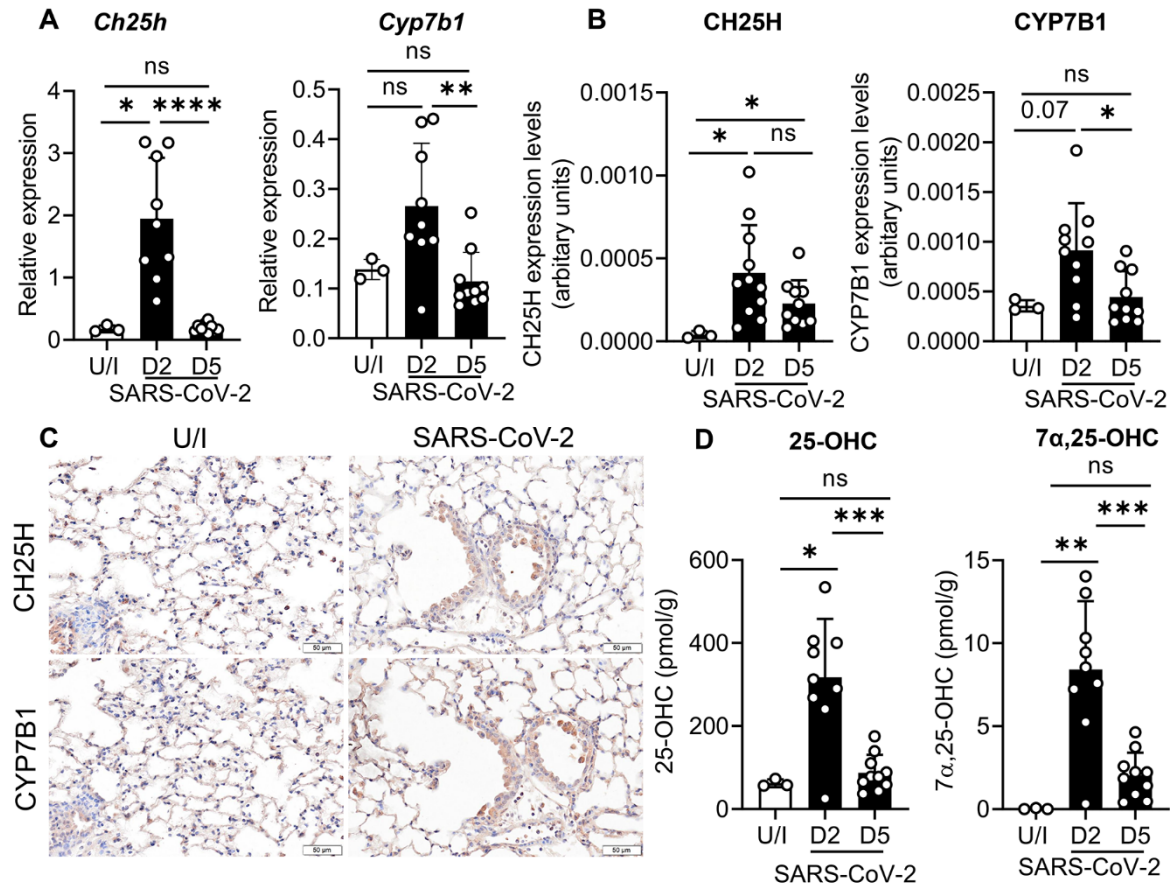
715 post-infection; U/I = mock infected; ns = not significant; *, $P < 0.05$; **, $P < 0.01$ indicate
716 significant differences.



717

718 **Figure 4. The GPR183 antagonist NIBR189 reduces inflammatory cytokine production.**
719 C57BL/6J and *Gpr183^{-/-}* mice were infected intranasally with 5,500 PFU of A/Auckland/01/09.
720 Mice were subsequently treated orally with 7.6 mg/kg NIBR189 or vehicle control twice daily
721 from 1 dpi until the end of the experiment. Cytokine measurements of **A) IL-6**, **B) TNF**, **C)**
722 IFN β and **D) IFN λ** at 7 dpi measured by ELISA. Data are presented as mean \pm SD of n=5-12
723 infected mice per genotype and timepoint. dpi = days post-infection; U/I = mock infected; ns
724 = not significant; *, $P < 0.05$; **, $P < 0.01$ indicate significant differences.

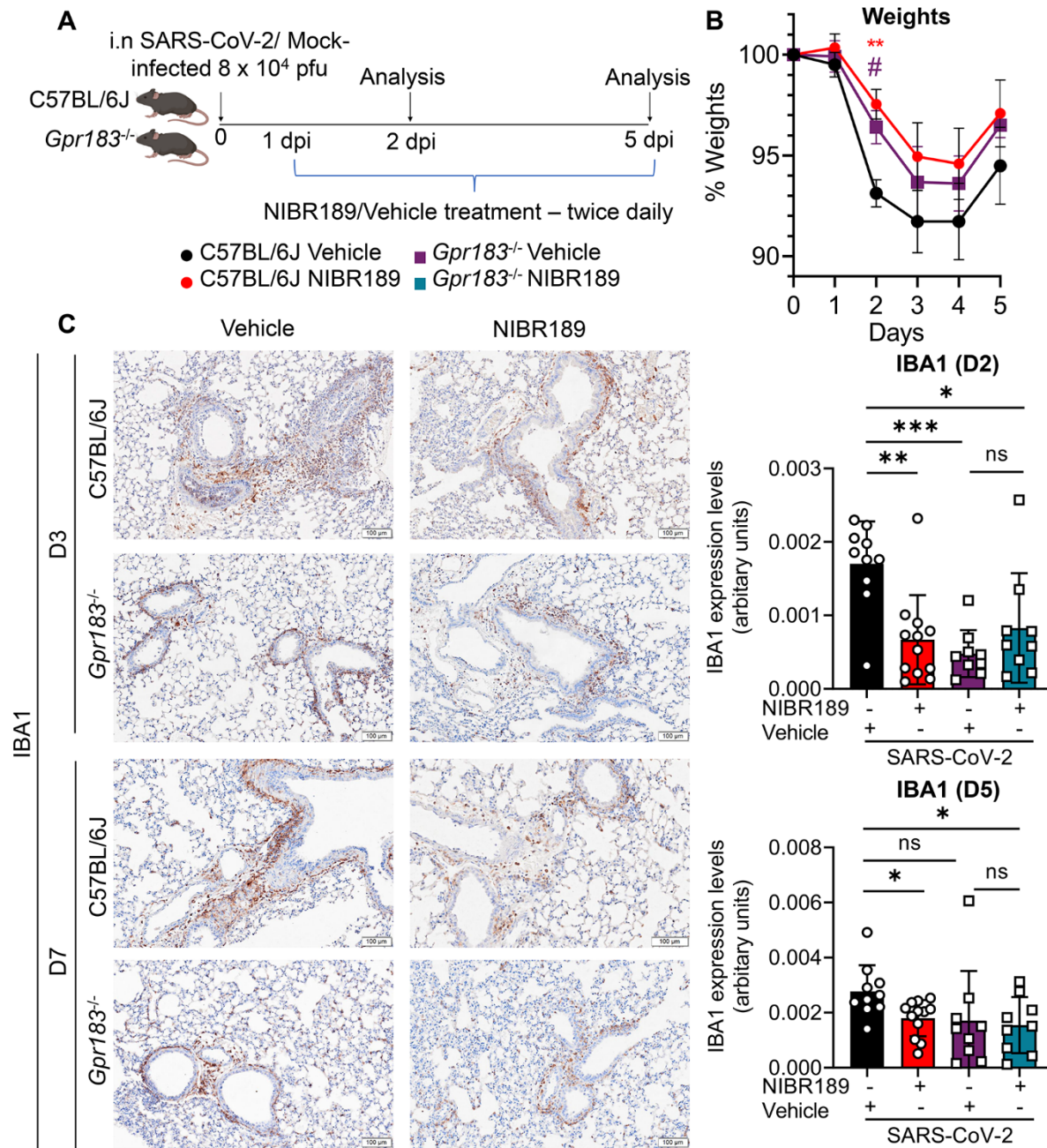
725



726

727 **Figure 5. SARS-CoV-2 infection leads to upregulation of CH25H and CYP7B1**
728 **expression in the lung and production of the oxysterols 25-OHC and 7α,25-OHC.**
729 C57BL/6J mice were infected intranasally with approximately 8×10^4 PFU of mouse-adapted
730 SARS-CoV-2. mRNA expression of **A) *Ch25h*** and ***Cyp7b1*** was measured by qRT-PCR at 2
731 dpi and 5 dpi normalized to *Hprt*. **B) Quantitative analysis of CH25H and CYP7B1 protein by**
732 IHC labelling and **C) representative IHC images of CH25H and CYP7B1** in lung sections in
733 uninfected, 2 dpi and 5 dpi. **D) Concentrations of 25-OHC and 7α,25-OHC** in the lungs at 2
734 dpi and 5 dpi expressed in pmol per gram lung tissue. Data are presented mean \pm SD of n=3
735 uninfected mice and n= 9-10 infected mice per timepoint. Scale Bar = 50μm; U/I = mock
736 infected; dpi = days post-infection; ns = not significant; *, P < 0.05; **, P < 0.01; ***, P < 0.001;
737 ****, P < 0.0001 indicate significant differences.

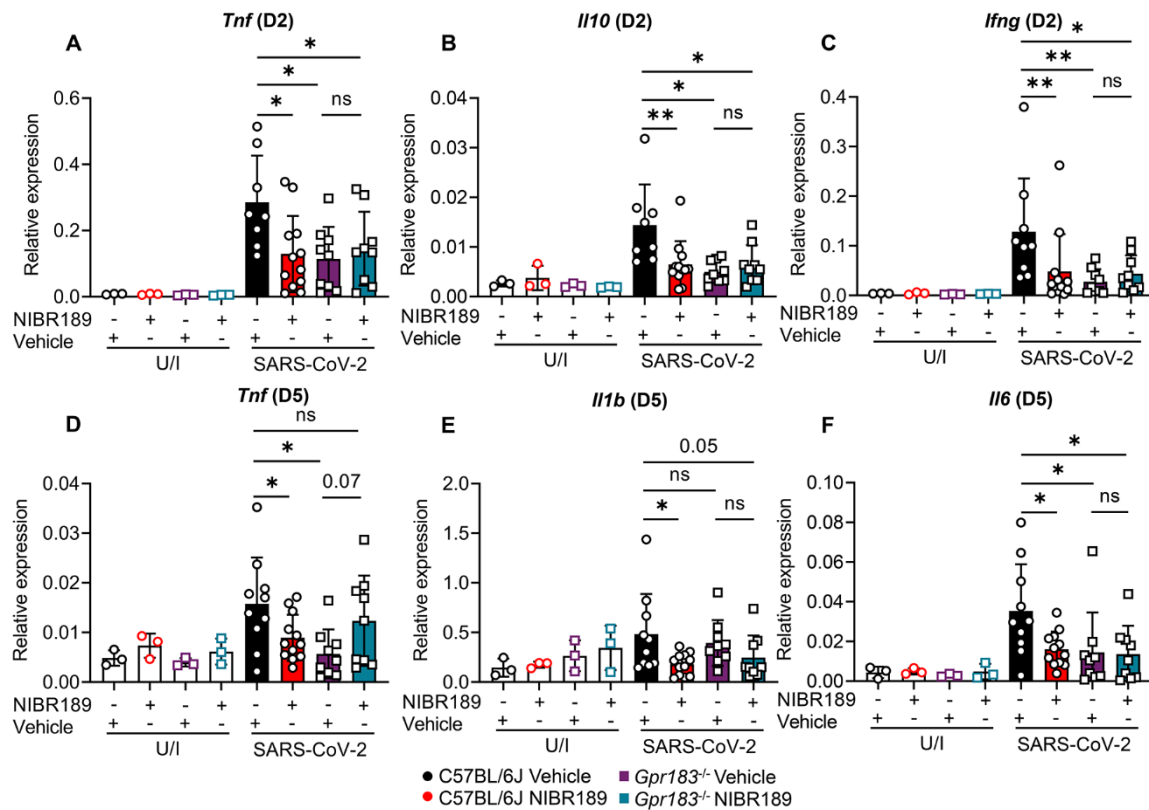
738



739

740 **Figure 6. GPR183 inhibition resulted in less SARS-CoV-2 infection-induced weight loss**
741 **and in reduced macrophage infiltration.** C57BL/6J and *Gpr183^{-/-}* mice were infected
742 intranasally with approximately 8×10^4 PFU of mouse-adapted SARS-CoV-2. Mice were
743 subsequently treated orally with 7.6 mg/kg NIBR189 or vehicle control twice daily from 1 dpi
744 until the end of the experiment. **A)** Experimental design. **B)** Weights of mice displayed as
745 percentage of the weight at time of inoculation. **C)** Representative IHC images of IBA1 in lung
746 of C57BL/6J and *Gpr183^{-/-}* mice with the respective treatment groups at 2 dpi and 5 dpi (left).
747 Scale Bar = 100μm. Quantitative analysis of IBA1 (right). Data are presented mean \pm SD of
748 n=9-12 infected mice per genotype and timepoint. Scale Bar = 100μm; U/I uninfected; dpi =

749 days post-infection; ns = not significant; *, $P < 0.05$; **, $P < 0.01$; ***, $P < 0.001$ indicate
750 significant differences.



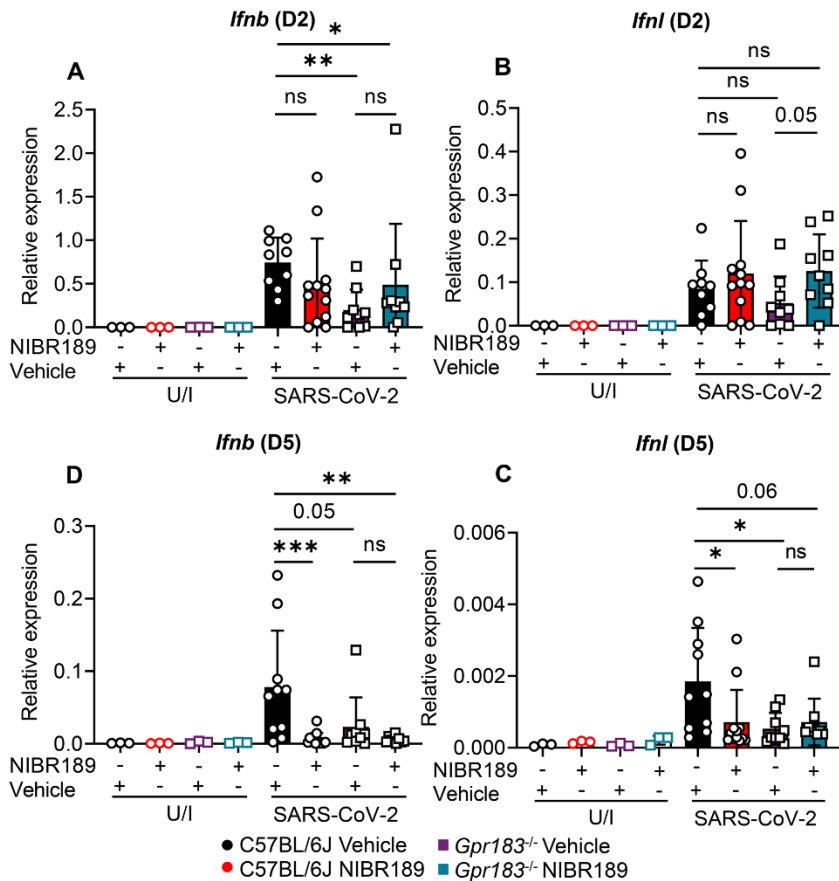
751

752 **Figure 7. GPR183 inhibition led to reduced inflammatory cytokine profile.** C57BL/6J
753 and *Gpr183*^{-/-} mice were infected intranasally with approximately 8×10^4 PFU of mouse-
754 adapted SARS-CoV-2. Mice were subsequently treated orally with 7.6 mg/kg NIBR189 or
755 vehicle control twice daily from 1 dpi until the end of the experiment. Relative expression of
756 **A) *Tnf*, B) *Il10*, C) *Ifng* at 2 dpi and D) *Tnf*, E) *Il1b*, F) *Il6* at 5 dpi** in the lungs measured by
757 RT-qPCR, normalized to *Hprt*. Data are presented mean \pm SD of n=3 uninfected mice and
758 n= 9-12 infected mice per genotype and timepoint. U/I = mock infected; dpi = days post-
759 infection; ns = not significant; *, $P < 0.05$; **, $P < 0.01$; ***, $P < 0.001$ indicate significant
760 differences.

761

762

763

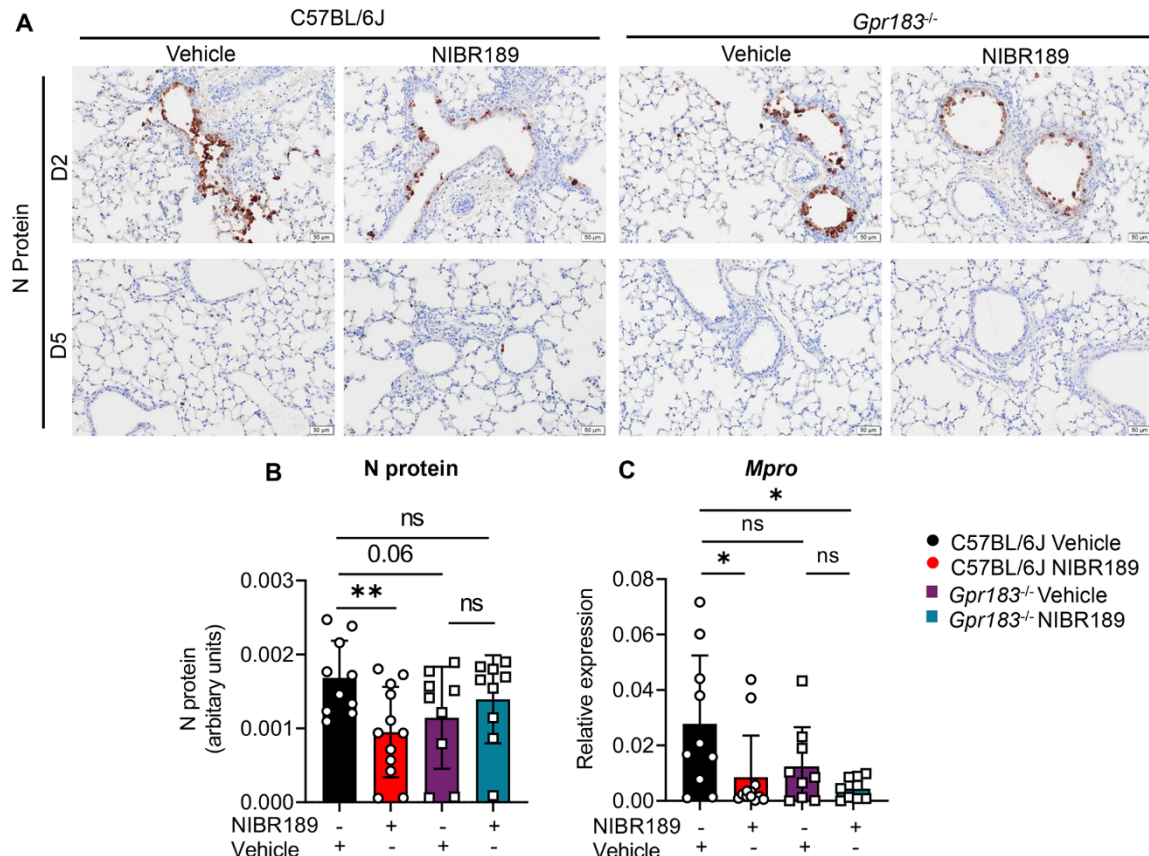


764

765 **Figure 8. GPR183 inhibition led to reduced interferon responses at 5 dpi.** C57BL/6J
766 and *Gpr183*^{-/-} mice were infected intranasally with approximately 8×10^4 PFU of mouse-
767 adapted SARS-CoV-2. Mice were subsequently treated orally with 7.6 mg/kg NIBR189 or
768 vehicle control twice daily from 1 dpi until the end of the experiment. Relative expression of
769 **A) *Ifnb*, B) *Ifnl* at 2 dpi and C) *Ifnb*, D) *Ifnl* at 5 dpi** in the lungs measured by RT-qPCR,
770 normalized to *Hprt*. Data are presented mean \pm SD of n=3 uninfected mice and n= 9-12
771 infected mice per genotype and timepoint. U/I = mock infected; dpi = days post-infection; ns
772 = not significant; *, P < 0.05; **, P < 0.01; ***, P < 0.001 indicate significant differences.

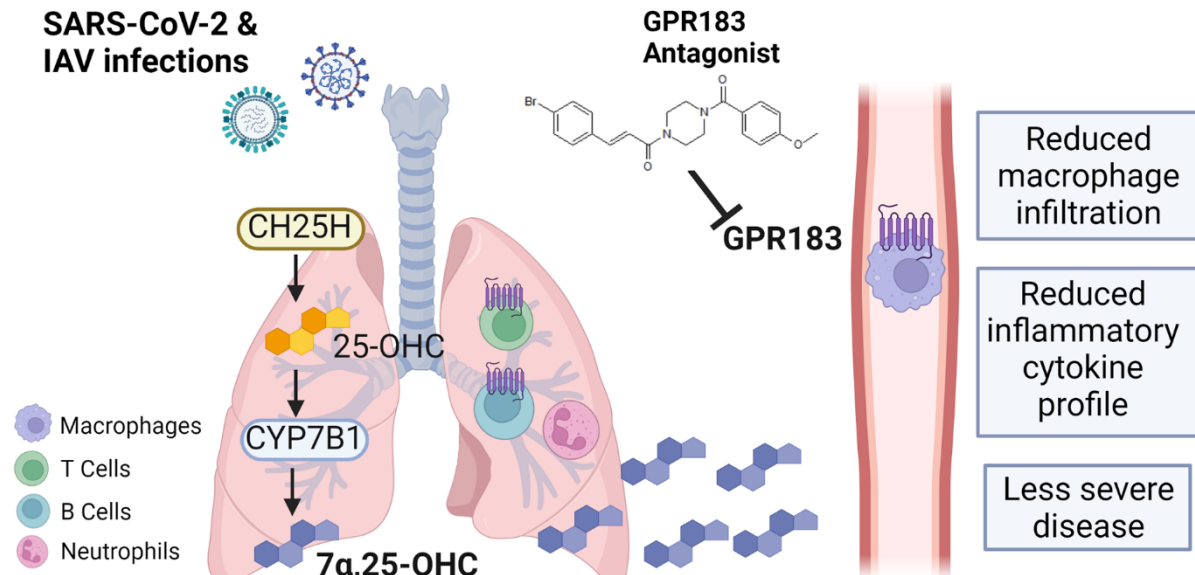
773

774



777 C57BL/6J and *Gpr183*^{-/-} mice were infected intranasally with approximately 8×10^4 PFU of
778 mouse-adapted SARS-CoV-2. Mice were subsequently treated orally with 7.6 mg/kg
779 NIBR189 or vehicle control twice daily from 1 dpi until the end of the experiment. **A**)
780 Representative IHC images of viral nucleocapsid (Np) expression at 2 dpi and 5 dpi. **B**)
781 Quantitative analysis of viral Np expression of the treatment groups at 2 dpi. **C**) Viral load
782 was assessed in the lung through the detection of *Mpro* RNA by RT-qPCR at 5 dpi,
783 normalized to HPRT. Data are presented mean \pm SD of n=9-12 infected mice per genotype
784 and timepoint. Scale Bar = 50 μ m; U/I = mock infected; dpi = days post-infection; ns = not
785 significant; *, P < 0.05; **, P < 0.01, indicate significant differences.

786



787

788 **Figure 10. Schematic figure of the role of GPR183 in the immune response to SARS-**
789 **CoV-2 and IAV infections.** SARS-CoV-2 and IAV infections lead to the upregulation of
790 CH25H and CYP7B1 which results in the production of 7 α ,25-OHC. This oxysterol
791 chemotactically attracts GPR183-expressing macrophages to the lungs where they produce
792 pro-inflammatory cytokines. Pharmacological inhibition of GPR183 attenuates the infiltration
793 of GPR183-expressing macrophages, leading to reduced production of inflammatory
794 cytokines without negatively affecting antiviral responses.

795

796

797

798

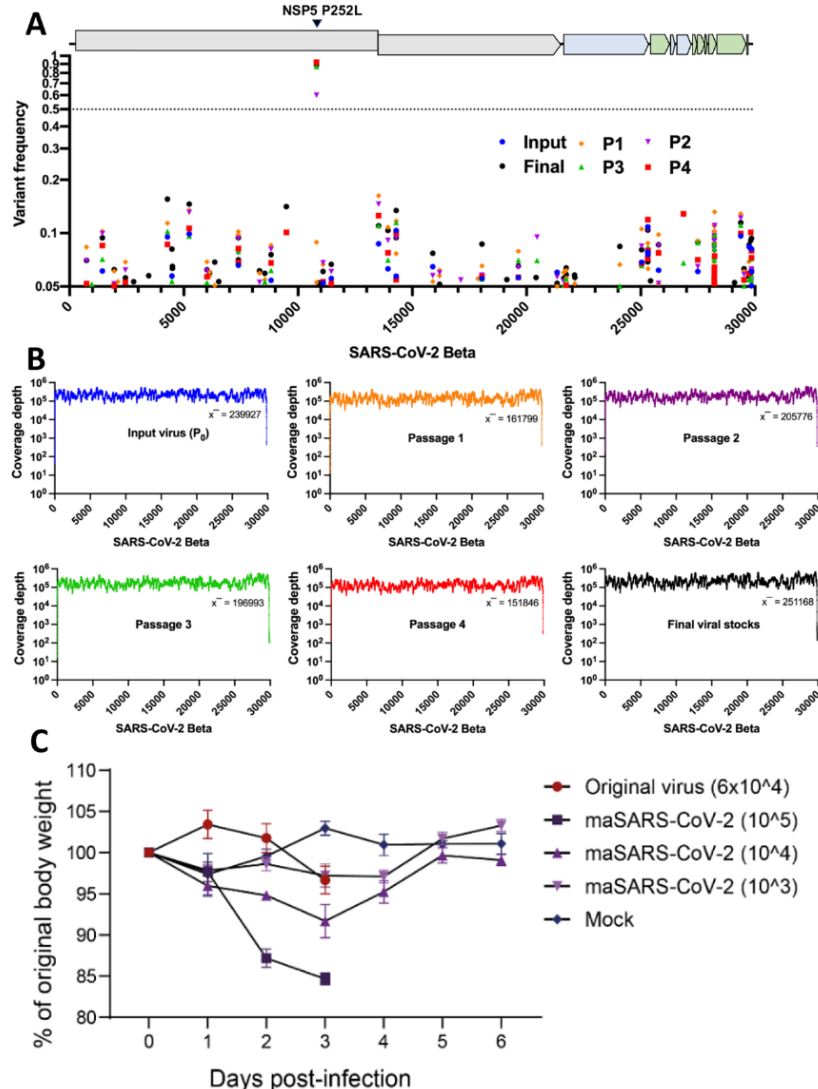
799

800

801

802

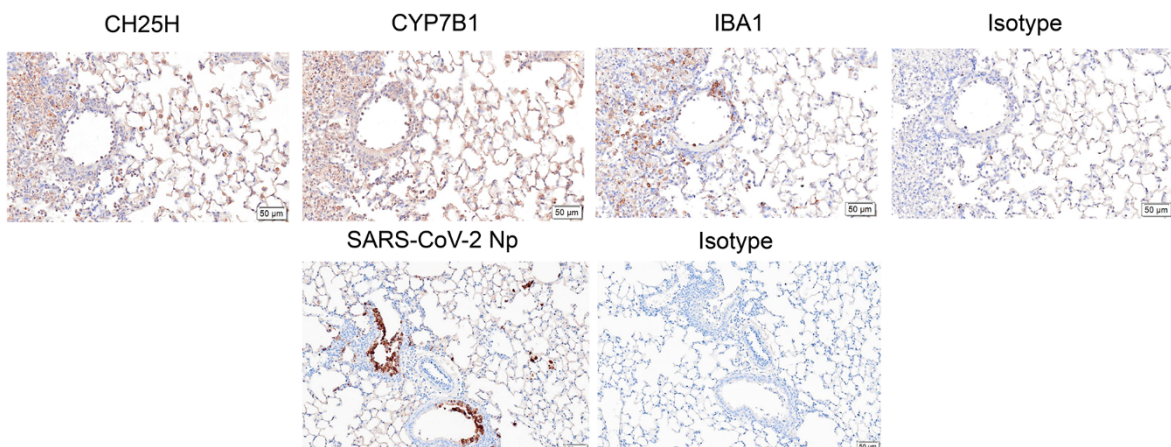
803



804

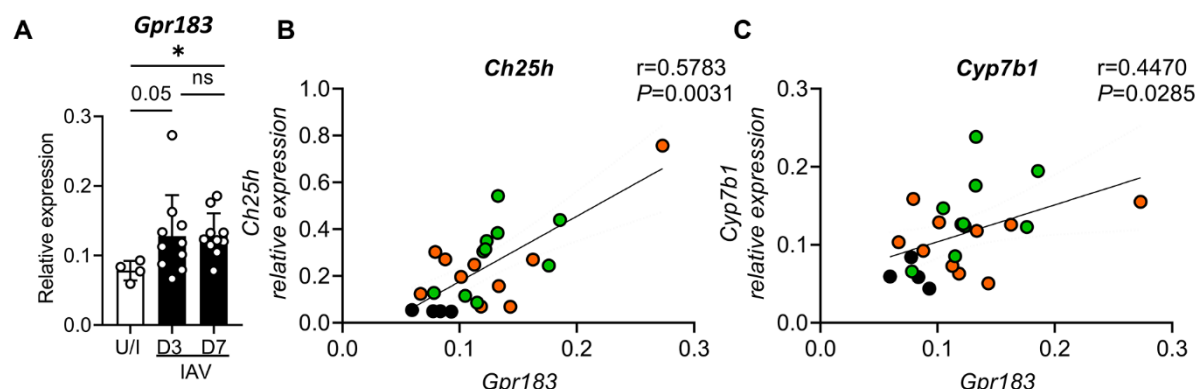
805 **Figure S1. Evolution and coverage of mouse-adapted SARS-CoV-2 virus. A)** Mutation
806 frequency of input SARS-CoV-2 Beta virus (blue circle) and passage one (orange diamond),
807 passage two (purple nabla), passage three (green triangle) and passage four (red square)
808 mouse-adapted viruses over the reference genome sequence as well as the final virus stocks
809 (black circle) amplified in VeroE6-hTMPRSS2 cells. The dotted line indicates the consensus
810 frequency of 0.5 **B)** Summary plots of read coverage of passaged SARS-CoV-2 viruses from
811 A) mapping to SARS-CoV-2 Beta strain. Depth of coverage of binary alignment files was
812 determined using samtools depth. **C)** Weight loss over time following infection with the Beta
813 variant of SARS-CoV-2 (original virus) or various doses of maSARS-CoV-2 (after four
814 passages in mice). Plaque forming units are indicated in brackets. Data indicates mean \pm
815 SEM.

816



817

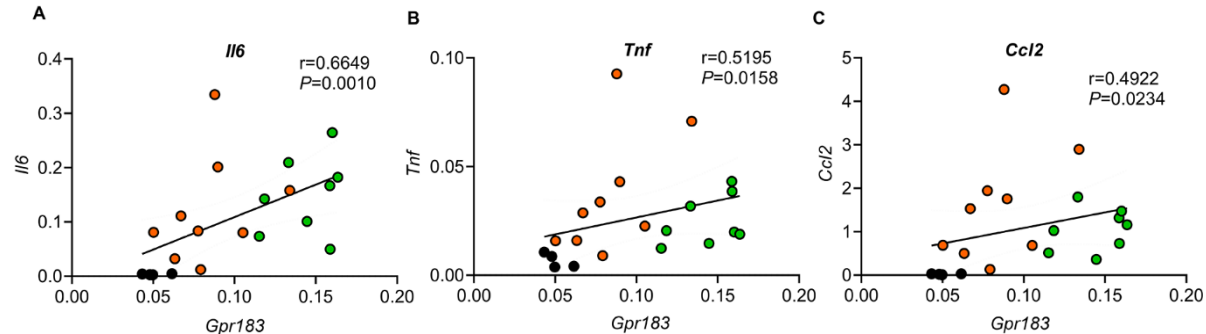
818 **Figure S2. Isotype staining controls for CYP7B1, CH25H, IBA1 and viral Np.** IHC of IAV-
819 infected lung sections incubated with rabbit anti-CH25H, rabbit anti-CYP7B, rabbit anti-IBA1
820 and an isotype-matched control (Rabbit IgG; negative control). IHC of SARS-CoV-2-infected
821 lung sections incubated with rabbit anti-SARS-CoV-2 nucleocapsid protein (Np) and an
822 isotype-matched control (Rabbit IgG; negative control). Scale bar = 50μm



823

824 **Figure S3. *Gpr183* mRNA expression is upregulated in the lung during IAV infection**
825 **and correlates with expression of the oxysterol synthesising enzymes CH25H and**
826 **CYP7B1.** C57BL/6J mice were infected intranasally with 5,500 PFU of A/Auckland/01/09. **A)**
827 Relative expression of *Gpr183* mRNA measured by RT-qPCR, normalized to *Hprt*.
828 Correlation analyses were performed with mRNA expression levels of *Gpr183* and oxysterol
829 synthesizing enzymes. Individual scatter plots showing correlations between *Gpr183* and **B)**
830 *Ch25h* and **C)** *Cyp7b1*. Black dots represent uninfected samples while coloured dots
831 represent IAV-infected samples (Orange dots, 3 dpi; green dots, 7 dpi). Data are presented
832 as mean ± SD of n=4 uninfected and n=8-10 infected mice per timepoint. ns = not significant;
833 *, P < 0.05 indicate significant differences. Spearman rank correlation test were used to

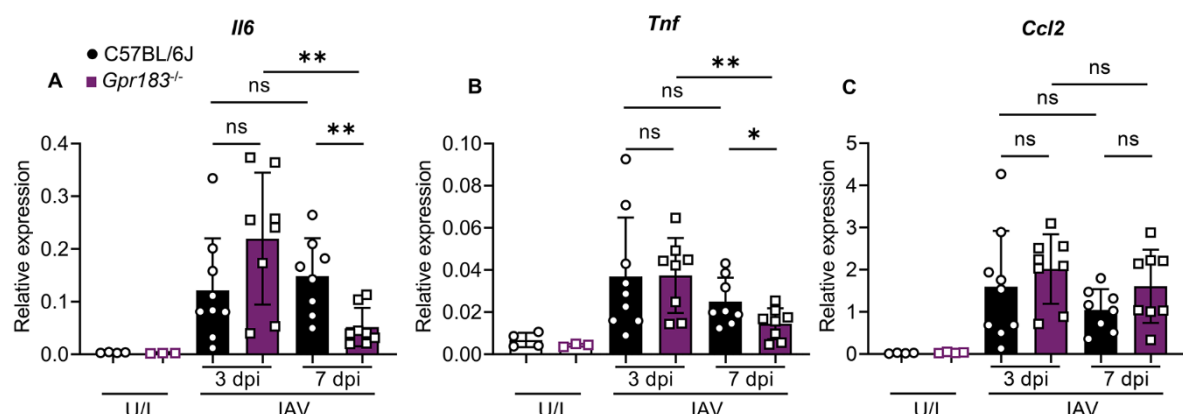
834 calculate correlation coefficient and to determine significant correlations with values
835 displayed on each scatter plot.



837 **Figure S4. Correlations between lung mRNA expression of *Gpr183* and inflammatory**
838 **markers in IAV-infected mice.**

839 Correlation analyses of *Gpr183* mRNA expression with mRNA expression of inflammatory
840 cytokines in lung tissue from IAV-infected C57BL/6J mice (n=21 pairs). Relative gene
841 expression was determined by RT-qPCR, normalized to *Hprt*. Individual scatter plots showing
842 correlations between *Gpr183* and **A) IL6**, **B) TNF** and **C) CCL2**. Black dots represent uninfected
843 samples while coloured dots represent IAV-infected samples (Orange dots, 3dpi; green dots,
844 7dpi). Spearman rank correlation test were used to calculate correlation coefficient and to
845 determine significant correlations with values displayed on each scatter plot.

846



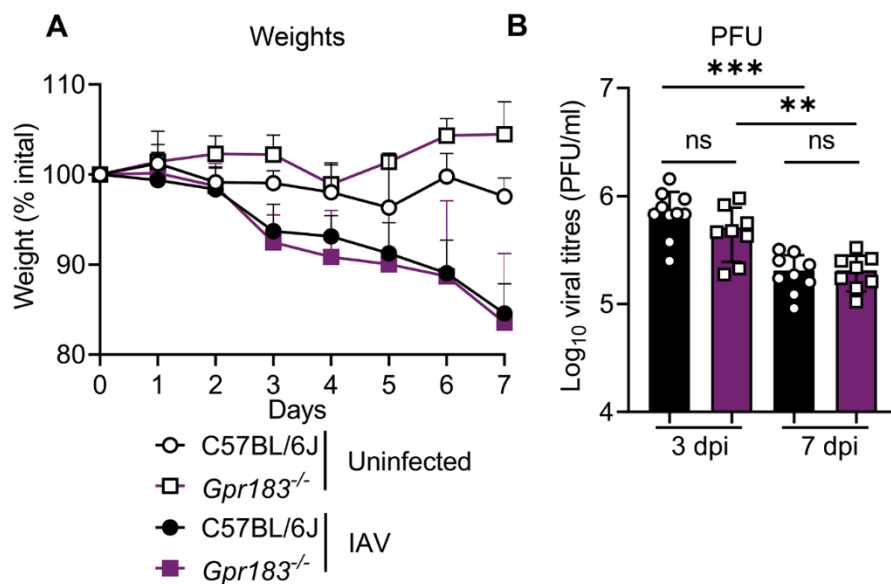
848 **Figure S5. Cytokine expression at mRNA and protein level in IAV-infected C57BL/6J**
849 **and *Gpr183*^{-/-} mice.** C57BL/6J and *Gpr183*^{-/-} mice were infected intranasally with 5,500 PFU
850 of A/Auckland/01/09. Cytokine measurements of **A) IL6**, **B) TNF** and **C) CCL2** at 3 dpi and 7 dpi
851 measured by RT-qPCR, normalized to *Hprt*. Data are presented as mean ± SD of n=4

852 uninjected per genotype and n=8-10 infected mice per genotype and timepoint. U/I =
853 uninjected; dpi = days post-infection; ns = not significant; *, $P < 0.05$; **, $P < 0.01$ indicate
854 significant differences.

855

856

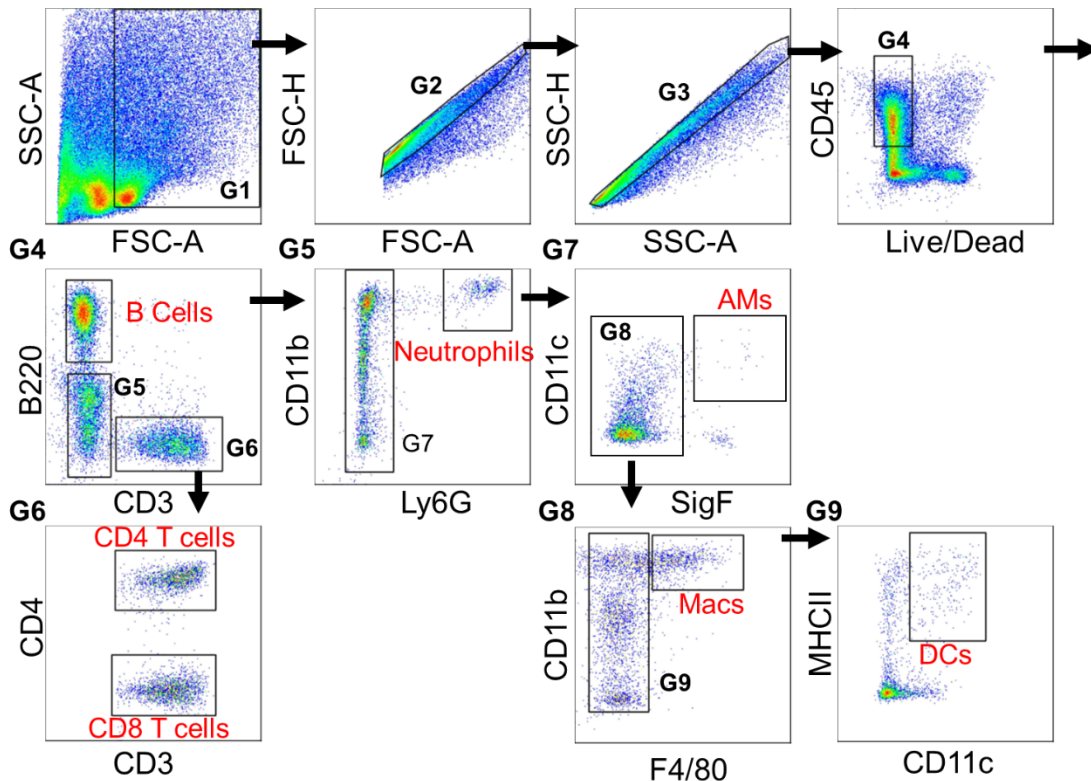
857



858

859 **Figure S6. Weights of IAV and mock infected C57BL/6J and Gpr183^{-/-} mice and viral**
860 **loads.** C57BL/6J and Gpr183^{-/-} mice were infected intranasally with approximately 5,500 PFU
861 of A/Auckland/01/09. **A)** Weights of IAV- or mock-inoculated mice are displayed as
862 percentage of the weight at time of inoculation. **B)** Viral load was assessed by measuring the
863 PFU by plaque assays. Data are presented as mean ± SD for n=8-10 infected mice per
864 genotype and timepoint. dpi = days post-infection; ns = not significant; **, $P < 0.01$; ***, $P <$
865 0.001 indicate significant differences.

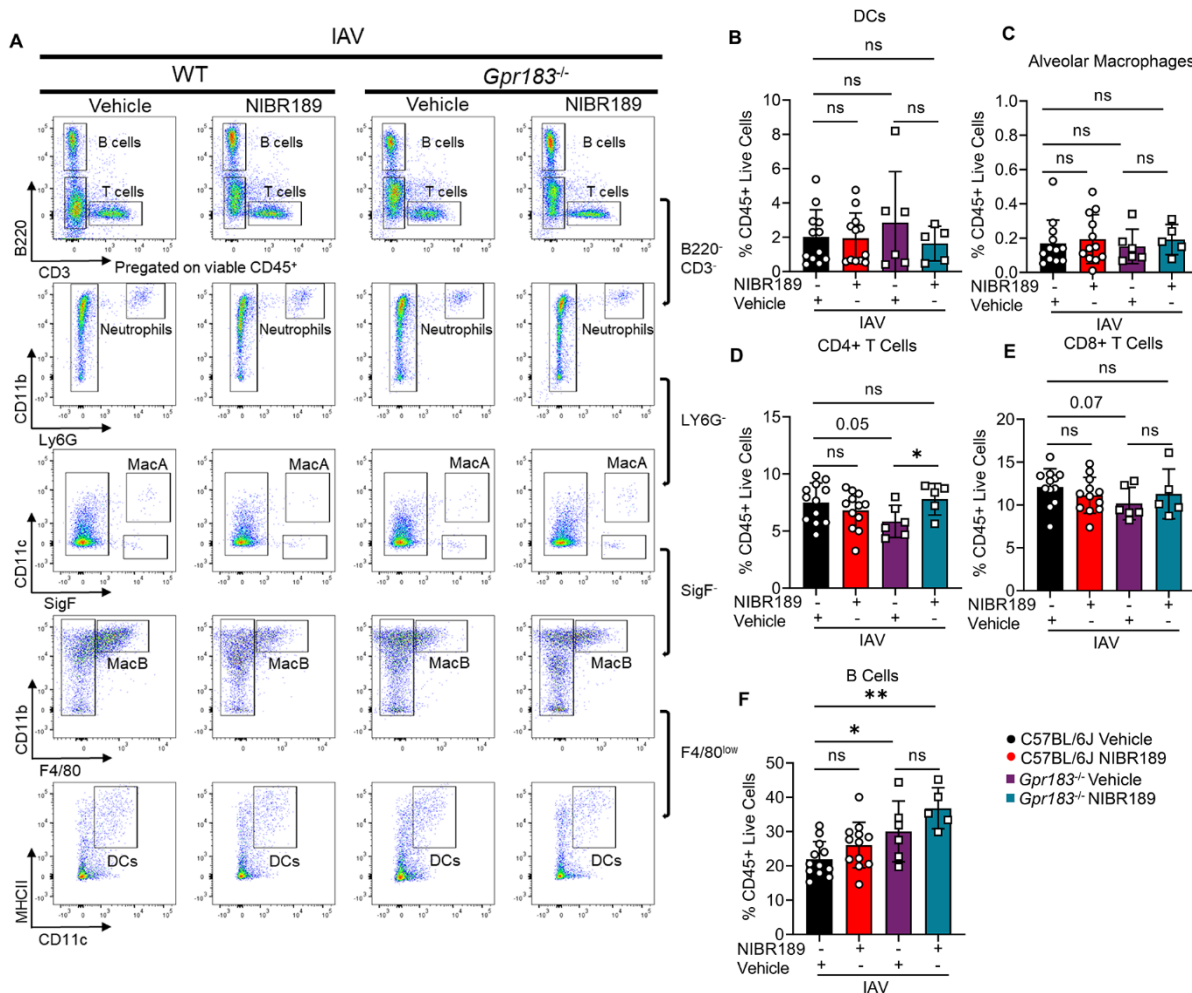
866



867

868 **Figure S7. Representative flow cytometry plots illustrating the gating strategy of**
869 **immune cells.** C57BL/6J or *Gpr183*^{-/-} mice were infected intranasally with 5,500 PFU of
870 A/Auckland/01/09. Mice were subsequently treated orally with 7.6 mg/kg NIBR189 or vehicle
871 control twice daily from 1 dpi until the end of the experiment. Gates containing multiple cell
872 populations are numbered (G1-G9). Gates that contained a single cell population are labeled
873 with its respective cell type. These includes: B cells (B220⁺; G5), CD4⁺ T cells (CD3⁺,CD4⁺;
874 G6), CD8⁺ T Cells (CD3⁺,CD4⁻; G6), Neutrophils (B220⁻,CD3⁻,Ly6G⁺; G5), Alveolar
875 macrophages (B220⁻,CD3⁻,Ly6G⁻,CD11c⁺,SigF⁺; G7), Macrophages (B220⁻,CD3⁻,Ly6G⁻,
876 ,SigF⁻,CD11b⁺,F4/80^{high}; G8) and Dendritic cells (DCs; B220⁻,CD3⁻,Ly6G⁻,SigF⁻,
877 F4/80^{low},CD11c⁺, MHCII⁺; G9).

878



879

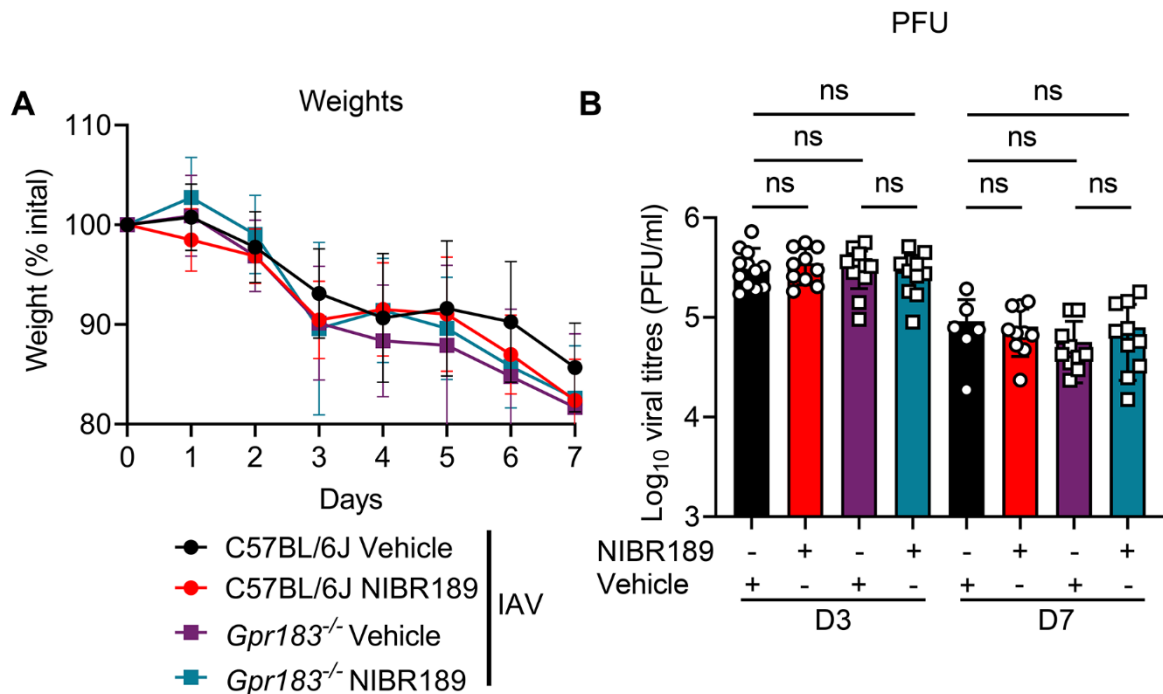
880 **Figure S8. Immune cell populations in the lungs of IAV-infected mice treated with the**
 881 **GPR183 antagonist NIBR189.** C57BL/6J or *Gpr183^{-/-}* mice were infected intranasally with
 882 5,500 PFU of A/Auckland/01/09. Mice were subsequently treated orally with 7.6 mg/kg
 883 NIBR189 or vehicle control twice daily from 1 dpi until the end of the experiment. **A)**
 884 Frequency of B cells (B220⁺), T cells (CD3⁺ CD8⁺ or CD4⁺), neutrophils (B220⁻CD3⁻Ly6G⁺)
 885 was determined by flow cytometry against total viable CD45⁺ immune cells at 3 dpi. Alveolar
 886 macrophages (CD11c⁺SigF⁺), infiltrating macrophages (F480^{high}/CD11b⁺/Ly6G⁻/SigF⁻) and
 887 dendritic cells (SigF⁻F4/80⁻MHCII⁺CD11c⁺) were further identified from the B220⁻CD3⁻Ly6G⁻
 888 cell population. **(B-G)** Graphs depicting the frequency of **B)** Dendritic cells, **C)** alveolar
 889 macrophages, **D)** CD4⁺ T cells, **E)** CD8⁺ T cells and **F)** B cells against total viable CD45⁺
 890 immune cells. Data are presented mean ± SD of n=5-12 infected mice per genotype and
 891 timepoint. UI = uninfected; dpi = days post-infection; ns = not significant.

892

893

894

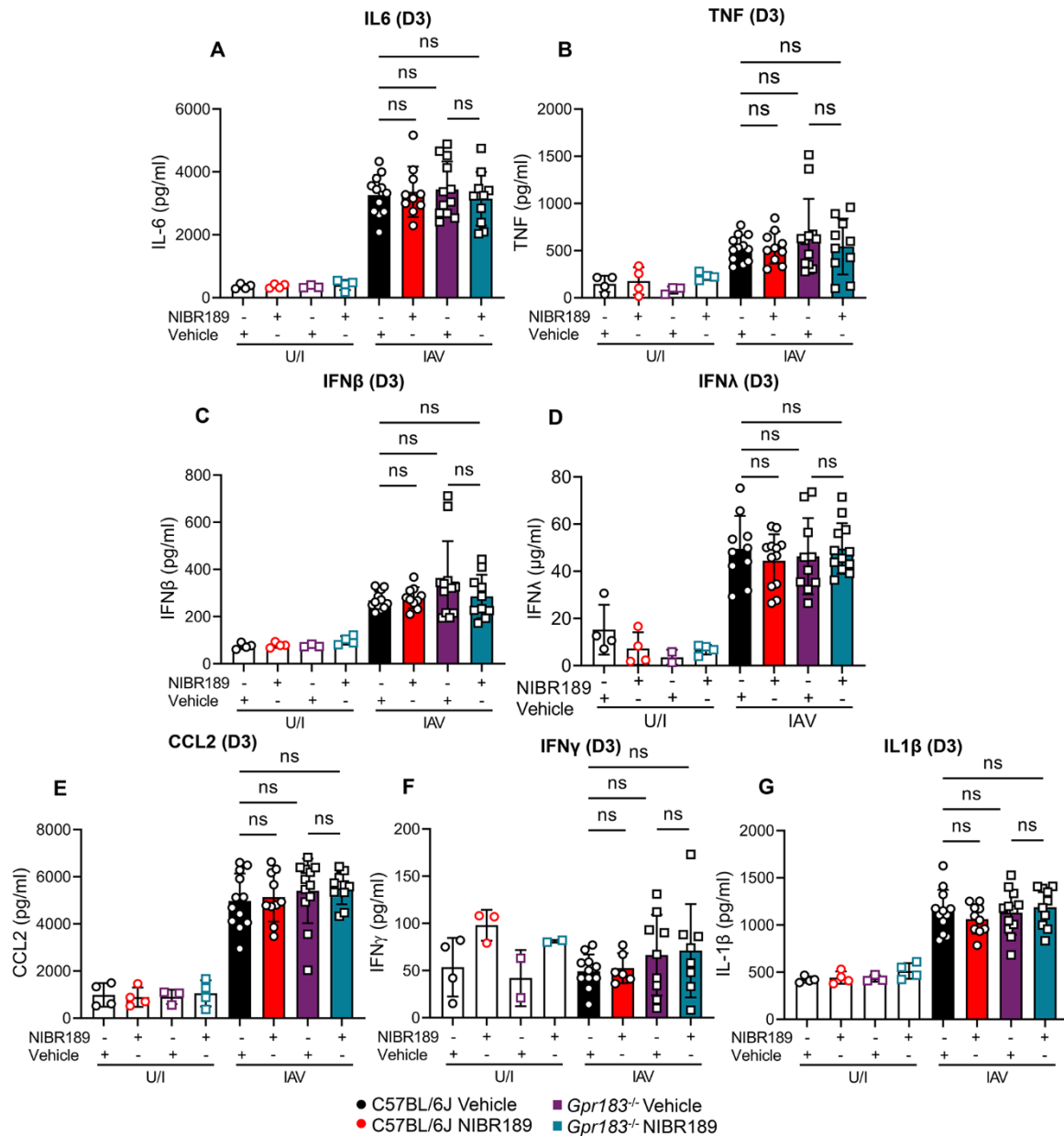
895



896

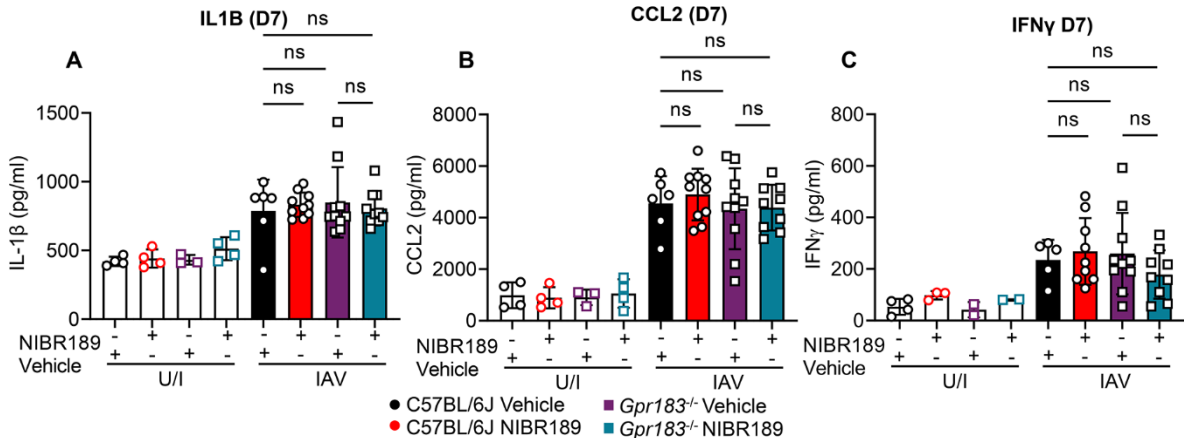
897 **Figure S9. Body weights and viral loads of IAV-infected C57BL/6J and *Gpr183*^{-/-} mice**
898 **treated with NIBR189 or vehicle.** C57BL/6J mice and *Gpr183*^{-/-} mice were infected
899 intranasally with 5,500 PFU of A/Auckland/01/09. Mice were subsequently treated orally with
900 7.6 mg/kg NIBR189 or vehicle control twice daily from 1 dpi until the end of the experiment.
901 **A)** Weights of IAV- or mock-inoculated mice with or without treatment are displayed as
902 percentage of the weight at time of inoculation. **B)** Viral load was assessed by measuring the
903 PFU through plaque assay. Data are presented mean \pm SD of n=6-12 infected mice per
904 genotype and timepoint. UI = uninfected; dpi = days post-infection; ns = not significant.

905



906

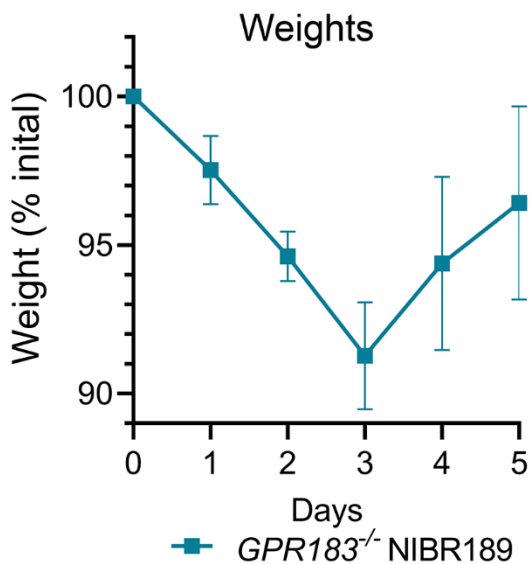
907 **Figure S10. Cytokine expression at protein level in IAV-infected C57BL/6J and Gpr183-/-**
908 **908 mice treated with NIBR189 and/or vehicle.** C57BL/6J and Gpr183^{-/-} mice were infected
909 intranasally with 5,500 PFU of A/Auckland/01/09. Mice were subsequently treated orally with
910 7.6 mg/kg NIBR189 or vehicle control twice daily from 1 dpi until the end of the experiment.
911 Cytokine measurements of **A) IL-6** **B) TNF**, **C) IFNβ**, **D) IFNλ**, **E) CCL2**, **F) IFNγ** and **G) IL-1β**, at 3 dpi measured by ELISA. Data are presented mean \pm SD of n=4 uninfected mice per
912 genotype and n=6-12 infected mice per genotype. U/I = uninfected; dpi = days post-infection;
913 ns = not significant. *, P < 0.05 indicate significant differences.



915

916 **Figure S11. Cytokine expression at protein level in IAV-infected C57BL/6J and Gpr183-
917 - mice treated with NIBR189 and/or vehicle.** C57BL/6J and *Gpr183* $^{-/-}$ mice were infected
918 intranasally with 5,500 PFU of A/Auckland/01/09. Mice were subsequently treated orally with
919 7.6 mg/kg NIBR189 or vehicle control twice daily from 1 dpi until the end of the experiment.
920 Cytokine measurements of **A**) IL-1 β , **B**) CCL2, and **C**) IFN γ at 7 dpi measured by ELISA.
921 Data are presented mean \pm SD of n=4 uninfected mice per genotype and n=6-12 infected
922 mice per genotype. U/I = uninfected; dpi = days post-infection; ns = not significant.

923

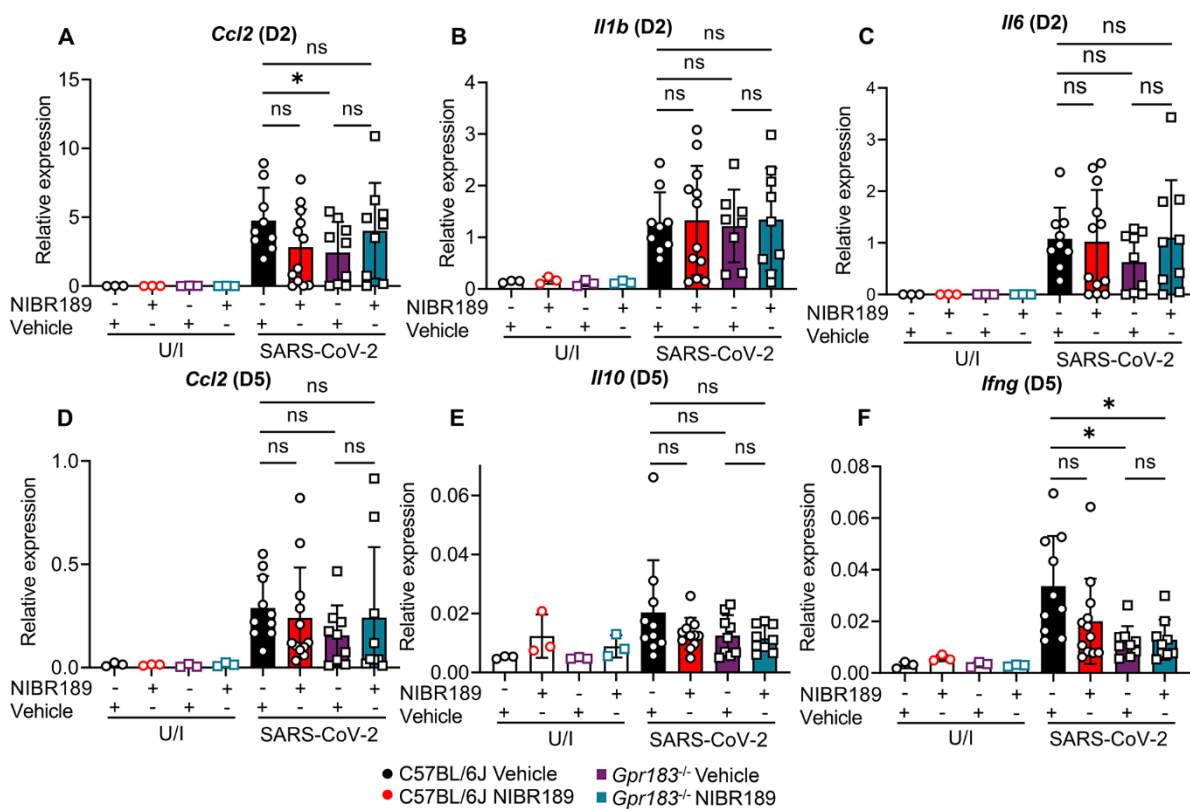


924

925 **Figure S12. GPR183 inhibition weight loss upon SARS-CoV-2 infection.** C57BL/6J and
926 *Gpr183* $^{-/-}$ mice were infected intranasally with approximately 8×10^4 PFU of mouse-adapted
927 SARS-CoV-2. Mice were subsequently treated orally with 7.6 mg/kg NIBR189 or vehicle
928 control twice daily from 1 dpi until the end of the experiment. Weights of mice displayed as
929 percentage of the weight at time of inoculation.

930

931



932

933 **Figure S13. Cytokine expression at mRNA in SARS-CoV-2-infected C57BL/6J and**
934 ***Gpr183*^{-/-} mice treated with GPR183 antagonist at 2 dpi and 5 dpi.** C57BL/6J and *Gpr183*
935 ^{-/-} mice were infected intranasally with approximately 8×10^4 PFU of mouse-adapted SARS-
936 CoV-2. Mice were subsequently treated orally with 7.6 mg/kg NIBR189 or vehicle control
937 twice daily from 1 dpi until the end of the experiment. Expression of **A) *Ccl2*, B) *Il1b* and C)**
938 ***Il6* at 2 dpi and D) *Ccl2*, E) *Il10* and F) *Ifng* 5 dpi** was measured by RT-qPCR normalized to
939 HPRT. Data are presented mean \pm SD of n=3 uninfected mice and n= 9-12 infected; mice
940 per genotype and timepoint. U/I = uninfected dpi = days post-infection; ns = not significant. *,
941 P < 0.05; **, P < 0.01; ***, P < 0.001 indicate significant differences.

942

943

944

945

946

947

948

949 **Table S1: Primers used in this study**

	Forward	Reverse
<i>Gpr183</i>	GTCGTGTTCATCCTGTGCTTCAC	TCATCAGGCACACCGTGAAAGTG
<i>Ch25h</i>	CTGACCTTCTTCGACGTGCT	GGGAAGTCATAGCCCCGAGTG
<i>Cyp7b1</i>	CGGAAATCTTCGATGCTCCAAAG	GCTTGTTCGAGTCCAAAAGGC
<i>Ccl2</i>	GCTACAAGAGGATACCCAGCAG	GTCTGGACCCATTCTTCTTGG
<i>Hprt1</i>	CCCCAAAATGGTTAACGGTTGC	AACAAAGTCTGGCCTGTATCC
<i>Ifnb1</i>	AACTCCACCAGCAGACAGTG	GGTACCTTGACCCCTCCAG
<i>Ifng</i>	CAGCAACAGCAAGGCGAAAAAGG	TTTCCGCTTCCCTGAGGCTGGAT
<i>Il10</i>	CGGGAAAGACAATAACTGCACCC	CGGTTAGCAGTATGTTGTCCAGC
<i>Il1b</i>	TGGACCTTCCAGGATGAGGACA	GTTCATCTCGGAGCCTGTAGTG
<i>Il6</i>	CTGCAAGTGCATCATCGTTGTT	TACCACTTCACAAGTCGGAGGC
<i>Ifnl</i>	AGCTGCAGGCCTTCAAAAAG	TGGGAGTGAATGTGGCTCAG
<i>Tnf</i>	TAGCCCACGTCGTAGCAAAC	ACAAGGTACAACCCATCGGC
<i>Hif1a</i>	CCTGCACTGAATCAAGAGGTGC	CCATCAGAAGGACTTGCRRGGCT
<i>mpro</i>	GAGACAGGTGGTTCTCAATCG	ACGGCAATTCCAGTTGAGC

950